



OPEN

Deep learning artificial neural network framework to optimize the adsorption capacity of 3-nitrophenol using carbonaceous material obtained from biomass waste

Rasikh Tariq¹, Mohamed Abatal^{2✉}, Joel Vargas³ & Alma Yolanda Vázquez-Sánchez⁴

The presence of toxic chemicals in water, including heavy metals like mercury and lead, organic pollutants such as pesticides, and industrial chemicals from runoff and discharges, poses critical public health and environmental risks leading to severe health issues and ecosystem damage; education plays a crucial role in mitigating these effects by enhancing awareness, promoting sustainable practices, and integrating environmental science into curricula to empower individuals to address and advocate for effective solutions to water pollution. However, the educational transformation should be accompanied with a technical process which can be eventually transferred to society to empower environmental education. In this study, carbonaceous material derived from *Haematoxylum campechianum* (CM-HC) was utilized for removing 3-nitrophenol (3-Nph) from aqueous solutions. The novelty of this research utilizes *Haematoxylum campechianum* bark and coconut shell, abundant agricultural wastes in Campeche, Mexico, for toxin removal, enhancing the adsorption process through artificial neural networks and genetic algorithms to optimize conditions and maximize the absorption efficiency. CM-HC's surface morphology was analyzed using scanning electron microscopy (SEM/EDS), BET method, X-ray powder diffraction (XRD), and pHpzc. Kinetic models including pseudo-first-order (PFO), pseudo-second-order (PSO), and Elovich were applied to fit the data. Adsorption isotherms were determined at varying pH (3–8), adsorbent dosages (2–10 g/L), and temperatures (300.15–330.15 K), employing Langmuir, Freundlich, Temkin, and Redlich–Peterson models. PSO kinetics demonstrated a good fit ($R^2 > 0.98$) for $C_i = 50$ – 100 mg/L, indicating a chemical adsorption mechanism. The Langmuir isotherm model exhibited the best fit, confirming chemical adsorption, with a maximum adsorption capacity (Q_m) of 236.156 mg/g at $T = 300.15$ K, $pH = 6$, contact time = 3 h, and 2 g/L adsorbent dosage. Lower temperatures favored exothermic adsorption. Artificial neural networks (ANNs) were employed for deep learning, optimizing the predictive model for removal percentage. Correlation heat maps highlighted positive correlations between time, dosage, and removal percentage, emphasizing the impact of initial concentration on efficiency. ANN modeling, incorporating iterative optimization, yielded highly accurate predictions, aligned closely with experimental results. The study showcases the success of deep learning in optimizing adsorption processes, emphasizing the importance of diverse correlation algorithms for comprehensive insights into competitive adsorption dynamics. The 5-14-14-1 deep learning architecture, fine-tuned over 228

¹Institute for the Future of Education, Tecnológico de Monterrey, Ave. Eugenio Garza Sada 2501, 64849 Monterrey, N.L., México. ²Facultad de Ingeniería, Universidad Autónoma del Carmen, Avenida Central S/N Esq. con Fracc. Mundo Maya, C.P. 24115 Ciudad del Carmen, Campeche, México. ³Instituto de Investigaciones en Materiales, Unidad Morelia, Universidad Nacional Autónoma de México, Antigua Carretera a Pátzcuaro No. 8701, Col. Ex Hacienda de San José de la Huerta, C.P. 58190 Morelia, Michoacán, México. ⁴Área Agroindustrial Alimentaria, Universidad Tecnológica de Xicotepec de Juárez, Av. Universidad Tecnológica No. 1000. Col. Tierra Negra Xicotepec de Juárez, 73080 Puebla, México. ✉email: mabatal@pampano.unacar.mx

epochs, demonstrated strong performance with mean squared error (MSE) values of 4.07, 18.406, and 6.2122 for training, testing, and total datasets, respectively, and high R-squared values. Graphical analysis showed a solid linear correlation between experimental and simulated removal percentages, emphasizing the need to consider more than just testing data for optimization. Experimental validation confirmed a 98.77% removal efficiency, illustrating the effectiveness of combining deep learning with genetic algorithms, and highlighting the necessity of experimental trials to verify computational predictions. It is concluded that the carbonaceous material from *Haematoxylum campechianum* waste (CM-HC) is an effective, low-cost adsorbent for removing 3-nitrophenol from aqueous solutions, achieving optimal removal at pH 6 and 300.15 K with a maximum adsorption capacity of 236.156 mg/g, following Langmuir model and pseudo-second order kinetics. The validated ANN model offers a reliable tool for practical applications in environmental remediation, advancing both environmental science and educational innovation by integrating artificial neural networks and data science methodologies into student learning experiences.

Keywords 3-nitrophenol, Carbonaceous materials, *Haematoxylum campechianum*, Deep learning, Artificial neural network, Genetic algorithm, Educational innovation, Higher education, Computational thinking, Artificial intelligence

The presence of toxic chemicals in water is a critical public health and environmental issue that poses serious risks to ecosystems and human health. Common water pollutants include heavy metals like mercury and lead, organic pollutants such as pesticides and pharmaceutical residues, and other industrial chemicals that can enter water supplies through agricultural runoff, industrial discharges, and inadequate waste management practices. The effects of these contaminants range from acute poisoning to long-term health issues like cancer, reproductive problems, and endocrine disruption. Education plays a pivotal role in addressing the challenges of water pollution by raising awareness about the sources and effects of contaminants and promoting sustainable practices¹. Through formal and informal educational programs², individuals and communities can learn about the importance of water conservation, pollution prevention, and the steps they can take to reduce their environmental footprint. Schools and universities can integrate environmental science into their curricula to equip tackle environmental challenges effectively^{3,4}. By fostering a deeper understanding of the impacts of toxic chemicals in water and the importance of water quality, education⁴ can empower individuals to participate in or advocate for conservation initiatives and policy changes.

In such case of nitrophenolic compounds, defined by their benzene frameworks adorned with hydroxyl and nitro functional groups, serve as crucial precursors across various industrial realms, including but not limited to, the synthesis of herbicides, pesticides, fungicides, along with the manufacture of paints, dyes, pharmaceuticals, and explosives⁵. This advisory stems from their pronounced toxicity, diminished biodegradability, propensity for bioaccumulation, and oncogenic potential^{6,7}.

The improper release of industrial wastewaters laden with nitrophenols (NPs) and their derivatives, even in minimal concentrations, poses significant risks to human health, wildlife, and plant life in aquatic ecosystems⁸. Regulation of phenolic compounds on different water matrices has been considered by several organizations. For example, U.S. Environmental Protection Agency establishes the maximum nitrophenol compounds level equal to 10 ng/L in natural water⁹. Moreover, the World Health Organization (WHO) establish the maximum levels of 0.009 and 0.2 mg/L for some phenolic compounds as pentachlorophenol and 2,4,6-trichlorophenol, respectively, in drinking water¹⁰.

In the case of rivers, lakes and related artificial or heavily modified water bodies, the European Union establish the maximum allowable concentrations of nonylphenol and pentachlorophenol equal to 0.002 and 0.001 mg/L, respectively¹¹. In Mexico, The Official Mexican Standard (NOM), regulates the phenolic compounds with a maximum allowed in drinking water of 9.0 µg/L¹². Previous studies have confirmed the presence of NP compounds in various environmental matrices, including groundwater¹³, precipitation^{14,15}, sediment deposits¹⁶, as well as in the atmosphere and industrial discharges¹⁷.

The urgent need for effective water purification strategies has led to the exploration of biosorbents for the removal of toxic contaminants from water. This approach is not only essential for protecting environmental health but also benefits from the integration of environmental education to enhance public awareness and involvement. Biosorbents, derived from biological materials, have demonstrated significant potential in adsorbing harmful substances from water. These natural adsorbents are advantageous due to their biodegradability, cost-effectiveness, and high efficiency in binding with various contaminants including heavy metals and dyes. Studies like those by Sarkar et al.¹⁸ and Tebbutt and Woods¹⁹ highlight the effectiveness of materials like modified clays, agricultural by-products, and engineered biochar in capturing and isolating pollutants from water bodies. Sarkar et al.¹⁸ specifically reviewed the water quality management in the Ganges river, emphasizing the role of biosorbents in mitigating heavy metal pollution. They also stressed the importance of integrating environmental education to improve water resource management and enhance the sustainability of such interventions.

Environmental education plays a pivotal role in enhancing the effectiveness of environmental remediation efforts by informing and engaging the public. For instance, Papavasileiou and Mavrakis²⁰ discussed projects implemented in Greek schools that focused on water-related issues, demonstrating how education can lead to better understanding and more proactive attitudes towards water conservation. Similarly, the work presented at the International Conference on New Water Culture by Mariolakos et al.²¹ used mythology to make environmental

education more accessible and engaging for students, thus fostering a deeper understanding of water's critical role in ecosystems.

Practical applications and case studies further illustrate the successful integration of biosorbents and education. The study by Sarkar et al.¹⁸ on the Ganges river utilized educational initiatives to inform and mobilize local populations about pollution control and the importance of maintaining water quality. These educational efforts are crucial in areas where industrial and agricultural activities heavily influence water quality, as they empower local communities to participate in sustainable practices.

In more recent studies, like that of Gebrekidan²², the systematic review of environmental education in Ethiopia revealed gaps in educational structures and emphasized the need for comprehensive educational frameworks to enhance environmental awareness and actions. This study highlights the necessity of embedding environmental education deeply within curriculums to cultivate a knowledgeable citizenry that can actively participate in environmental protection.

In order to remove NPs compounds or reduce its concentration from the wastewater, numerous researchers have developed various techniques such as membrane technology^{23,24}, chemical redox^{6,24}, adsorption^{24–26}, biodegradation^{24,27} and bioremediation²⁸. From the perspectives of operation, design, straightforwardness, and the ease with which adsorbent materials can be reused, the adsorption method stands out as significantly superior when contrasted with alternative approaches²⁴. However, the use of this technique has been restricted for large-scale treatment due to the high cost of adsorbents.

During a last decade, a significant research have been dedicated to the improvement of diverse varieties of cost-effective adsorbents aimed at eliminating phenolic compounds and other pollutants from water-based solutions^{25,29,30}. These efforts have highlighted the utilization of natural materials such as clay³¹, zeolite^{32,33}, and siliceous substances³⁴ for purification purposes. However, organic molecules removal was achieved by the modification of their external surface by surfactants^{32,35–37}.

The effectiveness of bioadsorbents, including *Phanerochaete chrysosporium*, the fungus *Pleurotus sajor-caju*, and *Sargassum*, in eliminating chlorophenols has demonstrated that the adsorption capacity is enhanced by the increase in the number of electronegative groups present^{38,39}.

The peak adsorption capability (q_m , mmol/g) for phenol, 2-chlorophenol, 4-chlorophenol, and 2,4,6-trichlorophenol when utilizing *Pleurotus sajor-caju* as the adsorbent was recorded at 0.95, 1.24, 1.47, and 1.89, respectively. This highlights not only the efficacy of the adsorbent but also its potential for being reused across more than five adsorption cycles without a significant loss in capacity³⁹. When treated with CaCl_2 , algal biomass was evaluated for its efficacy in removing chlorophenols, revealing that the maximum adsorption capacities (q_m values) for phenol, 2-chlorophenol, and 4-chlorophenol stood at 4.6 mg/g, 79 mg/g, and 251 mg/g, respectively.

Recently, activated carbon obtained from agriculture or industry residues has become a promising adsorbent to eliminate phenolic compounds because of its availability and the cheapness of precursor material. In the literature, it was reported the use of wood-based and lignite⁴⁰, olive stones⁴¹, apricot stone shells⁴², palm seed coat⁴³ based-activated carbon is used for the elimination of phenolic mixes. The phenols uptake was found to be depended of various factors, such as the superficial characteristic of the activated carbon, molecular dimension, acidity and the solubility of adsorbate.

Several research^{44–48} is now available which has focused on the usage of artificial intelligence models to improve the removal percentage, and it can contribute towards sustainability^{49,50}.

Sarang et al.⁵¹ delves into the effectiveness of a pseudo-emulsion hollow fiber strip dispersion technique in purifying industrial wastewater, with a particular emphasis on removing ethylparaben and diclofenac. This study employs an artificial neural network (ANN) as a predictive tool, estimating the success of the extraction process based on varied concentrations in the feed, carrier, and stripping phases, with extraction percentage being the key outcome measure. To assess the reliability of these models, statistical analyses such as root mean square error (RMSE) and mean absolute percentage error (MAPE) were utilized. The attainment of high regression values, 0.9956 for ethylparaben and 0.97562 for diclofenac, during the model training phase highlights the precision of the ANN in forecasting extraction outcomes. This precision suggests the method's applicability in the design and optimization of systems for treating industrial effluents.

Samadi-Maybodi et al.⁵² explore the removal of sarafloxacin (SRF), an antibiotic pollutant, from water bodies using a magnetized metal-organic framework ($\text{Fe}_3\text{O}_4/\text{MIL-101}(\text{Fe})$). The study applies response surface methodology (RSM) to determine optimal conditions for the adsorption of SRF, pinpointing an initial concentration of 10 ppm, a neutral pH of 7.0, an adsorbent amount of 20 mg, and a contact time of 40 min as the ideal parameters. The adsorption phenomena were found to align more accurately with the Langmuir isotherm model. In addition, the research developed an artificial neural network (ANN) to predict the removal efficacy of SRF, utilizing the Levenberg-Marquardt algorithm for model training. This model demonstrated significant predictive strength, showcased by high determination coefficients (R^2) during training (0.9995) and testing (0.9951) stages, alongside minimal mean squared errors (MSE), affirming its effectiveness as a predictive instrument for SRF adsorption rates.

El-Metwally et al.⁵³ introduce an innovative approach employing a novel fungal system for lipase biosynthesis with the aim of converting oily residues into biodiesel, using *Aspergillus flavipes* MH47297 to biosynthesize lipase from *Nigella sativa*, a by-product of agro-industrial processes. The study examines the influence of various factors such as cultural humidity, surfactant concentration, and inoculum density on lipase production, utilizing a Box-Behnken design (BBD) and ANNs in conjunction. This marked the inaugural application of ANNs in modeling the lipase biosynthesis process via semi-solid-state fermentation (SSSF). The optimized conditions predicted by the ANN closely matched the experimental outcomes, with the ANN model demonstrating superior precision over the BBD approach. Gas chromatography analyses confirmed the successful conversion of corn oil into biodiesel, illustrating the efficacy of the lipase produced.

The investigation by Sathishkumar et al.⁵⁴ explores the application of sophisticated machine learning techniques to evaluate the process of catalytic reduction in water tainted with dangerous nitrophenols and azo dyes. This study makes use of a catalyst composed of palladium oxide-nickel oxide to address pollutants like 4-nitrophenol, 2,4-dinitrophenol, 2,4,6-trinitrophenol, methylene blue, rhodamine B, and methyl orange. The effectiveness of this catalyst in diminishing these contaminants was scrutinized through experiments conducted over varying durations. To estimate the catalyst's performance, the research applied a range of machine learning models, including linear regression, support vector machines, gradient boosted machines, random forest, and XGBoost. The evaluation of these models was based on statistical measures such as root mean squared error, mean absolute error, and mean absolute percentage error. The findings demonstrated that the model using XGBoost provided the most precise predictions for 4-nitrophenol and 2,4-dinitrophenol, the model using random forest showed the highest efficacy for 2,4,6-trinitrophenol, methylene blue, and rhodamine B, and the model using support vector machines was particularly effective in predicting the reduction of methyl orange. Notably, the catalyst achieved a 98% reduction in a mixture of azo compounds within eight minutes, indicating its strong potential for real-life applications in water purification.

In a comprehensive review by Georgin et al.⁵⁵, the challenges and technological advancements in the remediation of 17 β -estradiol (E2) through adsorption are explored. E2, a potent endocrine disruptor, has been shown to adversely affect aquatic biota and ecosystem health even at low concentrations. Georgin et al. identify a range of adsorbents such as graphene oxides, nanocomposites, and carbonaceous materials that have been effectively employed to remove E2 from water. The review emphasizes that the efficiency of these adsorbents is influenced by factors such as the pH and temperature of the medium, with acidic to neutral pH and ambient temperatures around 298 K being most favorable. They highlight the relevance of the Langmuir and Freundlich models in describing the adsorption isotherms, indicating predominantly low-energy, physical interactions during E2 adsorption. The review calls for the establishment of stringent national and international standards for E2 removal, pointing out the economic and sustainability challenges in implementing these technologies at a large scale. Another significant study by Ahmad et al.⁵⁶ focuses on the adsorption of bisphenol A (BPA), a common pollutant from plastic production. They introduce a novel hyper cross-linked resin, ICYN-PPA, characterized by its high adsorption capacity and fast kinetics, achieving equilibrium within 350 min. This resin, synthesized from commercially available materials, shows a remarkable adsorption capacity of 112.8 mg.g⁻¹ for BPA. Notably, ICYN-PPA's thermal stability enhances its applicability in decontaminating BPA-laden effluents. The adsorption process, well represented by the Koble–Corrigan model, confirms the endothermic nature of the interaction, suggesting physical adsorption as the predominant mechanism. Gao et al.⁵⁷ investigated the removal of 4-nitrophenol (4-NP), a toxic byproduct of petrochemical industries, using MgCo-3D hydrocalcite nanospheres. These nanospheres, synthesized via the hot solvent method, displayed a maximum adsorption capacity of 131.59 mg.g⁻¹. The adsorption process, which predominantly involved hydrogen bonding and electrostatic interactions, adhered to the Langmuir, Redlich–Peterson, and Sips models, indicating a monolayer physical adsorption. Their study also demonstrated the excellent regeneration performance of the nanospheres, maintaining significant adsorption capacity after multiple cycles. In a study by Adebayo and Areo⁵⁸, a novel composite made from coconut shell and clay was used for the adsorption of phenol and 4-nitrophenol from wastewater. This composite showed exceptionally high adsorption capacities, particularly for phenol, with a Q_{\max} of 1665 mg.g⁻¹. The adsorption process, analyzed through various kinetic and equilibrium models, was best described by the Avrami fractional order and Liu isotherm. The study highlights the composite's effectiveness, achieving over 86% removal efficiency for the tested effluents, underlining its potential as a low-cost and efficient solution for treating industrial wastewater.

Khan et al.⁵⁹ conduct a detailed investigation into the potential of carbon material, sourced from the remnants of domestic fireworks, to capture Hexavalent chromium (Cr(VI)) from environments, a known toxic metal. This research meticulously examines how various factors, such as the length of the adsorption period, the acidity or alkalinity (pH) of the environment, the Cr(VI) solution's warmth, and its initial amount, impact the material's ability to adsorb the metal. To analyze, foresee, and enhance the adsorption mechanism, the study employs a sophisticated combination of response surface methodology and multiple regression analysis alongside an innovative artificial neural networks model integrated with particle swarm optimization. Findings from this integrated approach pinpoint the most effective adsorption scenario: a 94.7 min exposure period, with the Cr(VI) at 50.0 mg/L, at a temperature of 33.6 °C, and in a highly acidic setting (pH 2). This scenario reached an apex adsorption rate of 1.37 mg.g⁻¹. The study's analytical comparison reveals artificial neural networks' superiority in predicting outcomes over multiple regression analysis. Additionally, it aligns with the pseudo-first-order kinetic model in kinetic studies and identifies the Langmuir isotherm as the most accurate descriptor of this adsorption activity, indicating a primary reliance on physisorption. The thermodynamic analysis corroborates the adsorption's beneficial, spontaneous, and heat-absorbing characteristics.

Alatrasta and colleagues' research⁶⁰ systematically reviews 55 academic publications between 2011 and 2022, examining the role of metal-organic frameworks (MOFs) in phosphate adsorption processes. This comprehensive analysis indicates that the efficiency of MOFs in trapping phosphate relies on several critical elements, such as the particular variant of MOF used, its synthesis technique, any structural modifications made, and the conditions applied during its operational use. Despite the high theoretical capacity of many MOFs for phosphate adsorption, their practical application in phosphorus recovery over extended periods might be constrained due to the predominance of inner sphere complexation mechanisms. To predict the phosphate adsorption capacities effectively, the study employed machine learning techniques, particularly the use of artificial neural network (ANN) models, which took into account both operational parameters and synthesis characteristics. These models particularly emphasized the significance of the initial phosphate concentration and the use of modulator agents in the synthesis of MOFs.

Aghav and colleagues' study⁶¹ delves into predicting the adsorption competition between phenol and resorcinol on a variety of carbonaceous materials, including activated carbon, wood charcoal, and rice husk ash,

through the application of artificial neural networks. This investigation leverages a three-tiered feedforward neural network equipped with a backpropagation mechanism within MATLAB, aggregating data from 29 distinct batch experiments. Variables such as the amount of adsorbent used, initial phenol and resorcinol concentrations, the time span of contact, and the pH value were fed into the neural network to train it. The neural network then produces estimations on the efficiency of removing phenol and resorcinol. The precision of these artificial neural network predictions was rigorously evaluated using a suite of statistical indicators, including mean error, mean square error, root mean square error, and linear regression, all of which affirm the model's reliability in foreseeing the adsorption dynamics of these substances based on experimental data.

The novelty of this work is to use *Haematoxylum campechianum* barks and coconut shell which are one of the most abundant agricultural wastes in Campeche State in Mexico, therefore, the work make use of local products for the removal of harmful toxins. The objective of this work is to improve the adsorption capacity of activated carbons obtained from *Haematoxylum campechianum* bark and coconut shell as agriculture residues for the removal of 3-Nph from aqueous solutions by varying pH solution, contact time, dosage of adsorbent, concentration of 3-Nph, and temperature. Moreover, the study is enhanced by incorporating artificial neural networks, employing deep learning techniques to formulate an empirical regression model. Subsequently, data science methodologies and genetic algorithm optimization are applied to identify the optimal variable combination for maximizing the removal percentage. This distinctive approach sets this research apart from existing literature in the field.

Materials and methods

Chemicals

3-NpH was purchased from Sigma Aldrich ($C_5H_5NO_3$, MW = 139.11 g/mol, purity, 99.9%, CAS: 554-84-7). The stock solution was prepared by dissolving 1.0 g of 3-NpH in 1000 mL of deionized water and stored in a brown bottle. Solutions between 25 and 1000 mg/L used for further experiments were prepared by dilution of synthetic stock solution. 0.1 N of HCl or 0.1 N of NaOH solutions were prepared to adjust the solution pH from 3 to 8.

Preparation of carbonaceous material

The carbonaceous material was produced from *Haematoxylum campechianum* waste using the method described by Abatal et al.⁶². The bark of *Haematoxylum campechianum* was chopped, ground and sieved. The material was then washed several times with deionized water at 50 °C to remove any residues and finally dried in an oven at 70 °C for 12 h. After pre-treatment, the material was dried in a deionized water oven at 50 °C for 12 h. The material was then washed several times with deionized water at 50 °C to remove any residues.

After pre-treatment, 50 g of *Haematoxylum campechianum* was placed in contact with 250 ml of H₃PO₄ at 50 °C for 3 h (chemical activation), then the filtered solid was dried at 70 °C for 12 h. The heat treatment was carried out at 50 °C for 12 h. The heat treatment was carried out as follows: 50 g of impregnated *Haematoxylum campechianum* was introduced into a muffle at 500 °C for 60 min, at 10 °C/min. The sample was then cooled to 25 °C. The carbonaceous material was washed with a 5% NaHCO₃ solution to remove the residual H₃PO₄ and then with deionized water until the pH of the filtrate reached a value of 6–7. Finally, the carbonaceous material from *Haematoxylum campechianum* (CM-HC) was dried at 110 °C for 12 h and then stored in a closed glass bottle and placed in a desiccator.

Characterization techniques

The point zero of charge (pH_{pzc}) of CM-HC was determined adding 0.1 g of each adsorbent to 50 mL of NaCl 0.01 M solution at previously adjusted pH value ($pH_{initial}$). Solutions pH of were adjusted from 2 to 12 by adding a drop of 0.1 N of HCl or 0.1 N of NaOH. The sample was agitated for 24 h at ambient temperature. Then, the samples were filtered and final solution pH (pH_{final}) of each solution was measured. CM-HC sample was characterized by X-Ray Diffraction methods. The X-ray patterns were collected on an APD-2000 diffractometer using CuK α radiation at room temperature in a range $2\theta = 5^\circ - 70^\circ$. Surface characteristics of CM-HC sample was studied by scanning electron microscopy (SEM) technique was performed to study the superficial structure of the samples before and after adsorption.

Sorption study

In this study, removal of 3-NpH by CM-HC was carried out using batch method. For kinetic study, the experiments were done by addition a mass 0.05 g of CM-HC to 10 mL of 3-NpH at different initial concentrations in a conical tube and agitated at 200 rpm in a multitube shaker apparatus (Model CVP-0228—Cyrilab). Initial concentrations of 3-NpH were 50 mg/L, 100 mg/L and 250 mg/L and contact time was varied from 5 to 1440 min. All tests were carried out in triplicate and the mean value was used in all cases.

After each contacted time at $T = 300.15$ K and $pH = 6$, the samples were centrifuged for 5 min at 4500 rpm (Centrifugent CRM Globe) in order to separate the adsorbent from aqueous phase. Before to measure the final concentrations of 3-Nph, absorbance (Abs.) of the samples with initial concentrations (Ci) of 3-Nph from 2 to 20 mg/L were measured using UV–visible spectrophotometer (Thermo Scientific Evolution 201/220) at $\lambda = 273$ nm. Calibration curve was obtained by the plotting of Abs. vs. Ci which gave a good correlation coefficient ($R^2 = 1$).

The sorption capacity (q_t , mg/g) and the removal efficiency (%) were calculated using the Eqs. (1) and (2), respectively:

$$q_t = \frac{C_i - C_t}{m} V \quad (1)$$

$$\%removal = \frac{C_i - C_t}{C_i} * 100 \quad (2)$$

Where C_i (mg/L) is the initial concentration, C_t (mg/L) is the concentration at time t (min), q_t (mg/g) is the adsorption capacity, V (L) is the volume and m (g) is the mass of the adsorbent.

Table 1 gives the experimental conditions used to investigate the effects of contact times, solution pH, temperature, and dosage of adsorbents on the removal of 3-Nph.

Kinetic models

In order to investigate the mechanism involved in the adsorption of 3-Nph on CM-HC, experimental data were evaluated using four kinetic models, the pseudo-first order (PFO), pseudo-second order (PSO), and Elovich. The equations of PFO, PSO, and Elovich models are expressed by the Eqs. (3), (4), (5) respectively.

$$q_t = q_e (1 - \exp(-k_1 t)) \quad (3)$$

$$q_t = \frac{k_2 q_e^2 t}{1 + k_2 q_e t} \quad (4)$$

$$q_t = \frac{1}{\beta} \ln(1 + \alpha \beta t) \quad (5)$$

Where q_e (mg/g) and q_t (mg/g) are the amounts of 3-Nph adsorbed at equilibrium and at time t (min) respectively. k_1 ($\frac{1}{min}$) and k_2 ($\frac{g}{mgmin}$), are the rate constants of pseudo-first, pseudo-second order, and intraparticle diffusion models respectively. β is the constant related to the extent of surface coverage (g/mg) and α is the theoretical adsorption capacity (mg/g.min).

Isotherm models

Experimental data were examined using nonlinear forms of the Langmuir, Freundlich, Temkin, and Redlich–Peterson isotherm models Eqs. (6), (7), (8), (9).

$$q_e = \frac{q_m K_L C_e}{1 + K_L C_e} \quad (6)$$

$$q_e = K_F C_e^{1/n} \quad (7)$$

$$q_e = B_T \ln(A_T C_e) \quad (8)$$

$$q_e = \frac{K_{RP}}{1 + \alpha_{RP} C_e^\beta} C_e \quad (9)$$

where q_e and q_m are the solid phase sorbate concentration in equilibrium (mg/g), C_e is the equilibrium sorbate concentration in liquid phase (mg/L), K_F is Freundlich constant (L/g) and $1/n$ is the heterogeneity factor. K_{RP} (L/g), α_{RP} (L/mg) and β are Redlich–Peterson isotherm constants. β is the exponent which lies between 1 and 0. In this study, solver add-in of Microsoft Excel was used to optimized the variance between the experimental data and predicted isotherms.

Error functions

Despite the use of coefficient of determination (R^2) by many studies to provide the best fitting, the nonlinear fits of kinetic and isotherm models were analyzed against the experimental data using error functions in order to verify the suitable model for the adsorption system. In this study, six error functions including the average

Experiments	Experimental parameters				
	pH	Time(min)	Ci(mg/L)	Dosage (g/L)	T (K)
Contact times	6	15–1440	50–250	5	300.15
Solution pH	3–8	1440	25–1000	5	300.15
Temperature	6	1440	25–1000	5	300.15–330.15
Dosage	6	1440	25–1000	2–10	300.15

Table 1. Values of contact times, solution pH, temperature and adsorbent dosage parameters used for experimental process.

relative error (ARE), sum of square error (SSE), normalized standard deviation, Δq (%), Chi-square test (χ^2), sum of absolute error (EABS), and root mean square error (RMSE) have been calculated employing the equations 10, 11, 12, 13, 14 and 15 respectively⁶³.

$$ARE = \sum_{i=1}^n \frac{1}{N} \frac{|(q_{e,exp} - q_{e,cal})|}{q_{e,exp}} * 100 \quad (10)$$

$$SSE = \sum_{i=1}^n (q_{e,exp} - q_{e,cal})^2 \quad (11)$$

$$\Delta q(\%) = 100 \sqrt{\frac{1}{N-1} \sum_{i=1}^n \left(\frac{q_{e,exp} - q_{e,cal}}{q_{e,exp}} \right)^2} \quad (12)$$

$$\chi^2 = \sum_{i=1}^n \frac{(q_{e,exp} - q_{e,cal})^2}{q_{e,cal}} \quad (13)$$

$$EABS = \sum_{i=1}^n |(q_{e,exp} - q_{e,cal})| \quad (14)$$

$$RMSE = 100 \sqrt{\frac{1}{N-2} \sum_{i=1}^n (q_{e,exp} - q_{e,cal})^2} \quad (15)$$

where $q_{e,exp}$ (mg/g) is the experimental adsorption capacity obtained from the Eq. (1) and $q_{e,cal}$ (mg/g) is the calculated adsorption capacity obtained from the nonlinear forms of PFO and PSO kinetic models or isotherm models (Langmuir and Freundlich), and n is the number of experimental data points.

Adsorption and desorption study

The recovery of 3-Nph and the regeneration of the adsorbent material are very important in adsorption processes, sustainability and cost-effectiveness of adsorbents. For this purpose, three adsorption/desorption cycles were carried out using NaOH solution as desorbing agent. For the adsorption step, 100 mg of CM-HC were mixed in Erlenmeyer flasks with 50 mL of 3-Nph at 100 mg/L (Ci), and stirred for 24 h at $T = 300.15$ K. The mixture was then filtered and the final concentration of 3-Nph (Cf) in the supernatant was determined by UV-vis spectrophotometric analysis.

The quantity of 3-Nph adsorbed after contact with AB-HC was calculated using Eq. (1).

For desorption process, 50 mL of 0.2 M NaOH was added to 3-Nph-loaded CM-HC. The mixture was agitated at 300.15 K for 24 h. After this time, the sample was filtered and the residual concentration of 3-Nph was measured.

The quantity of 3-Nph desorbed Q_{des} (mg/g) was calculated using this equation Eq. (16)

$$q_{des} = \frac{C_{des}V}{m} \quad (16)$$

Where, C_{des} (mg/L) is the concentration of 3-Nph after desorption, V (L) is the volume of NaOH solution, m (g) is the mass 3-Nph-loaded CM-HC.

The regenerated CM-HC was rinsed for several time with deionized water and dried at 105 °C for 2 h before the next cycle of adsorption/desorption.

Results and discussions

Characterization of CM-HC

Figure 1 shows that the point of zero charge of CM-HC equal to 6.5. This result is similar with those obtained from other precursor materials such as *Dipterocarpus alatus* ($pH_{pzc} = 6.3$)⁶⁴, rice husk ($pH_{pzc} = 6.8$)⁶⁵. Therefore, when the solution pH is above than the pH_{pzc} ($pH > pH_{pzc}$), the surface of CM-HC is negatively charged and the cationic species will be preferentially removed, whereas values of pH are below than pH_{pzc} ($pH < pH_{pzc}$), the charge of the surface of CM-HC will become positive and then anionic species are preferentially attracted via electrostatic interactions⁶⁶.

XRD diffraction pattern of CM-HC is presented in Fig. 2. It can be observed that HCAC has a semicrystalline structure related to the amorphous region between 10 and 40° corresponding to the carbonic fraction due to the preparation and characterization of activated carbons from different precursors⁶⁷.

Scanning electron microscope (SEM) analysis was carried out in order to investigate physical surface morphology of CM-HC. The SEM micrographs of CM-HC (Fig. 3) show that the particles of the synthesized activated carbon have a rough surface and an irregular shape with a variety of randomly distributed cavities which can

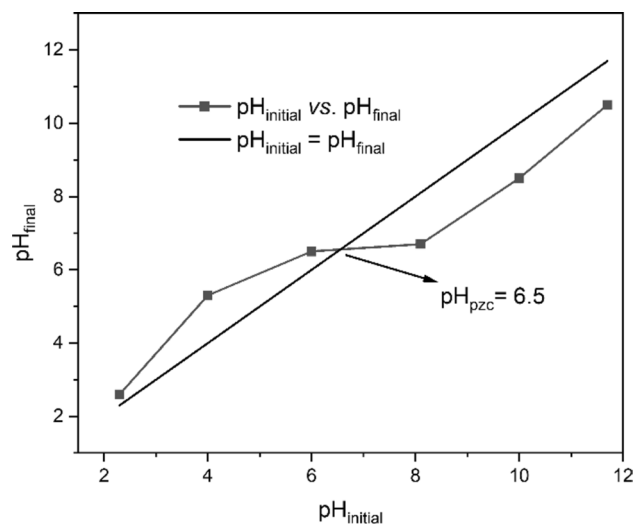


Fig. 1. pH_{pzc} of CM-HC.

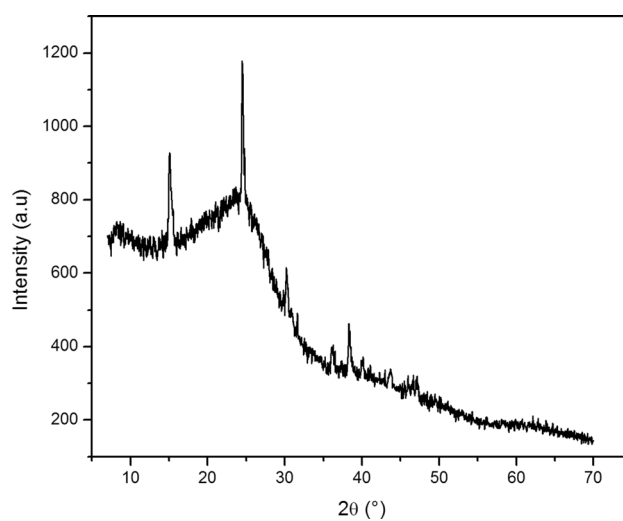


Fig. 2. XRD pattern of CM-HC.

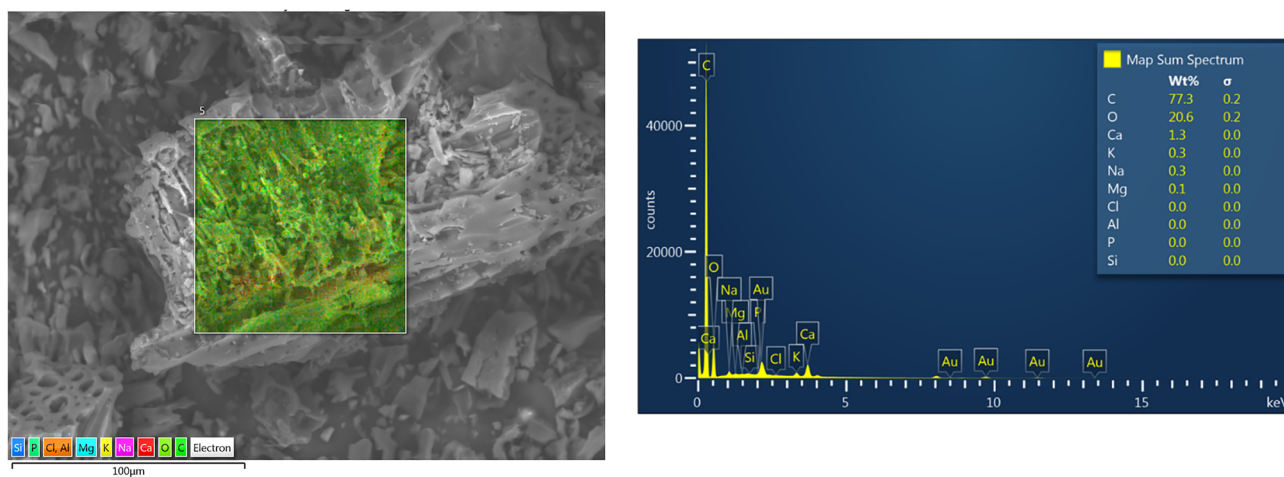


Fig. 3. SEM images and EDS analysis of CM-HC.

provide easy access transport toward the adsorption sites⁶⁸. The elemental composition of the activated carbon was performed by energy dispersive X-ray spectroscopy (EDS) is also shown in Fig. 3. In CM-HC, the material consists predominately of carbon and oxygen, the summary of these two elements to be 97.9% per weight. The rest of the composition (2.1%) corresponds to metallic fractions (Ca, K, Na and Mg).

The mean pore diameter of CM-HC calculated by BET equations were 2.1382, with a surface area of 124.15 m²/g. The difference in the surface properties can be attributed to the type of biomass precursor. Beker et al., reported that the adsorption of phenols is carried out in ultramicropores and micropore with diameters between 0.7 and 2 nm⁶⁹. Therefore, it is suspected that both adsorbents can be usefully used for removal of 3-nitrophenol from aqueous solution, due to the smaller molecular diameter of 3-Nph (0.6202 nm)⁷⁰.

Sorption study

Adsorption isotherms at different solution pH

The study of pH effect on the removal of 3-Nph on MC-HC was performed at ambient temperature by adjusting the solution pH of 3-Nph at 3, 6 and 8. For each solution, initial concentration was varied from 25 to 1000 mg/L.

Usually, at low pH values, anions are favorably adsorbed on the sorbent surface due to the presence of high concentration of H⁺ ions, while at high pH values, cations are more adsorbed on the sorbent surface as a result of high concentration of OH⁻ ions⁷¹. In addition, it well known that the degrees of dissociation and ionization of organic compounds as well as the adsorbent surface charge depended to the pH solution⁷², therefore, it is important to study the effect of pH solution on the adsorption of 3-Nph on MC-HC.

Figure 4a–c show the adsorption isotherms of 3-Nph on MC-HC at initial pH 3, 6 and 8, respectively. It can be seen that the adsorption capacity increases between pH 3 and 6, and then decreases for pH 8. This suggests that, the interaction of 3-Nph with CM-HC is more favorable in the acid than alkaline medium. In previous researches, the uptake for phenols in certain pH range present a dome-shaped curve^{25,73}, which is attributed to the change in nature of adsorbent (surface charge) and adsorbate species at different pH⁶⁹.

At pH between 3 and 6, the surface of CM-HC is positively charged (pH_{pzc} (CM-HC) = 6.7). Furthermore, in this pH range, 3-Nph mainly present as neutral species (pK_a (3-Nph) = 8.3 at 298 K), however the concentration

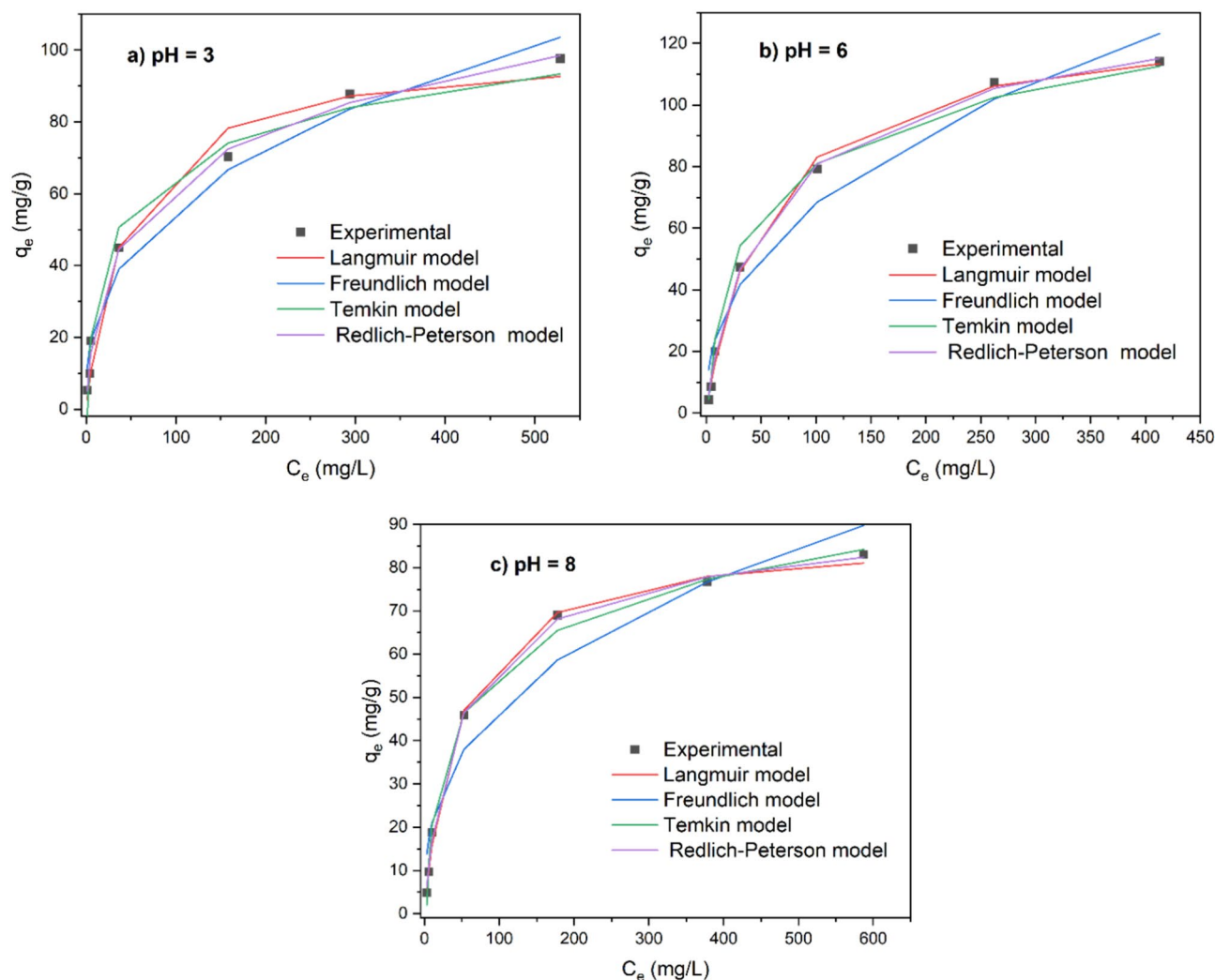


Fig. 4. Plot of adsorption isotherms for 3-Nph on MC-HC at (a) pH = 3, (b) pH = 6 and (c) pH = 8.

of its anionic form ($C_6H_5NO_3^-$) increases with increasing of solution pH and as consequently higher uptakes at pH = 6 compared to pH = 3, by means of electrostatic attractions between the surface charged positively and the anionic form of 3-NpH^{74,75}. At pH = 8, the uptake of 3-Nph declined. This result can be attributed to the electrostatic repulsion force between the surface of CM-HC negatively charged and the abundance anionic form of 3-Nph. Previous investigations have reported similar behavior of phenol^{143,69,73,76}, nitrophenols (2,4-dinitrophenol, 3-nitrophenol, 4-nitrophenol)^{42,76,77} and chlorophenols (2,4-dichlorophenol, 2-chlorophenol, 4-chlorophenol)^{42,76} adsorption on activated carbons.

Nonlinear equations of Langmuir, Freundlich, Temkin, and Redlich-Peterson isotherm models were used to investigate the adsorption mechanism. Table 2 shows the equation's parameters with their respective correlation coefficients (R^2).

The results indicate that the Langmuir and Redlich-Peterson models were well described the adsorption data for CM-HC in the pH range studied with R^2 values between 0.9805 and 0.9985 compared to Freundlich model ($0.9454 \leq R^2 \leq 0.9767$) and Temkin ($0.9768 \leq R^2 \leq 0.9954$). This result suggests the formation of multilayers on the adsorbent surface where the interaction between phenols and surface of carbonaceous materials is due Van der Waals' forces and π - π interactions⁴². As shown in Table 2, the maximum adsorption capacities, q_{max} calculated from Langmuir isotherm model were 100.523, 128.625, and 87.284 mg/g, at pH = 3, 6, and 8, respectively. The values of Redlich-Peterson exponential constant, β are close to unity (0.794–0.944), this indicates that the Redlich-Peterson model reduces to the Langmuir model⁷⁸.

As can be seen from Table 3, the calculated values of error functions APE, SSE, Δq (%), χ^2 , EABS and RMSE from the experimental data were lowest for Langmuir and Redlich-Peterson than Temkin and Freundlich isotherms. This result proves the applicability of Langmuir and Redlich-Peterson isotherm models to describe the adsorption mechanism of 3-Nph on CM-HC.

Isotherm Model	Parameters	pH		
		3	6	8
Langmuir	q_{max} (mg/g)	100.523	128.625	87.284
	K_L (L/mg) (10^{-2})	2.222	0.018	0.022
	R^2	0.9805	0.9974	0.9974
	N	2.738	2.393	2.806
Freundlich	K_F (mg/g)(L/mg) ^{1/n}	10.487	9.945	9.255
	R^2	0.9767	0.9634	0.9454
Temkin	B_T (L/mg)	15.966	22.476	15.636
	A_T (KJ/mol)	0.654	0.363	0.371
	R^2	0.9768	0.9865	0.9954
Redlich-Peterson	α_{RP} (L/mg)	0.175	0.036	0.036
	K_{RP} (L/g)	4.940	2.760	2.234
	β	0.794	0.916	0.944
	R^2	0.9958	0.9985	0.9985

Table 2. Langmuir, Freundlich, Temkin, and Redlich-Peterson isotherm parameters for the adsorption of 3-Nph on CM-HC at different solution pH.

pH	Model	Error functions					
		APE	SSE	Δq (%)	χ^2	EABS	RMSE
3	Langmuir	17.466	168.721	0.280	10.634	25.801	5.809
	Freundlich	32.242	201.919	0.576	8.463	33.964	6.355
	Temkin	18.970	128.320	0.317	4.894	26.796	5.066
	Redlich-Peterson	9.735	36.662	0.174	1.910	13.184	2.708
6	Langmuir	8.279	33.754	0.118	1.274	12.653	2.598
	Freundlich	57.478	469.224	1.052	16.197	54.511	9.687
	Temkin	10.216	99.680	0.151	2.364	21.640	4.465
	Redlich-Peterson	11.266	19.640	0.187	1.191	11.201	1.982
8	Langmuir	5.980	16.848	0.093	0.796	9.010	1.836
	Freundlich	45.364	358.738	0.834	13.418	43.813	8.470
	Temkin	14.117	29.922	0.259	4.633	12.551	2.446
	Redlich-Peterson	8.078	9.938	0.136	0.713	7.716	1.410

Table 3. Values of error functions of adsorption isotherm models of 3-Nph on CM-HC at different solution pH.

Effect of contact time on adsorption equilibrium

The study of adsorption kinetics was done at ambient temperature without any adjustment of solution pH. Figure 5a–c show respectively the adsorbed amount of 3-NpH (mg/g) by MC-HC versus contact time (min) with 3-NpH initial concentration (C_i) at 50, 100 and 250 mg/L. It can be seen that within 120 min, 80.1%, 81.7%, and 65.3% of 50, 100, and 250 mg/L of 3-NpH were removed. The higher rate of 3-NpH adsorption in this first stage can be attributed to the availability of adsorption site on the adsorbent surface⁷⁹. After this time, adsorption capacity was gradually increased as increase contacted time reaching equilibrium, which varied from 180 to 360 min depending to initial 3-NpH concentration (the faster equilibrium time was found for $C_i = 50$ mg/L). This result can be attributed to the more availability of the uncovered surface area of the adsorbents at low solute concentrations^{76,80}. In this study, the equilibrium time was found to be minor compared to other equilibrium times reported by other studies for the removal of phenols using different carbonaceous materials⁸¹. For $C_i = 50$, 100, and 250 mg/L, the adsorption capacity reached 8.97, 17.38, and 41.37 mg/g, at equilibrium time, respectively. Experimental data were analyzed using nonlinearized equations of pseudo-first-order (PFO), pseudo-second-order (PSO), and Elovich kinetic models. Table 4 displays the kinetic parameters of PFO (k_1 , q_e), PSO (k_2 , q_e), and Elovich (α, β) with their corresponding correlation coefficients R^2 .

The results showed in Table 4 indicate that for $C_i = 50$ and 100 mg/L, pseudo-second order model displays higher coefficient regression ($R^2 = 0.9840, 0.9892$) in comparing to pseudo-first-order (0.9043, 0.8744) and Elovich ($R^2 = 0.8182, 0.8839$) models. Also, it can observe that the calculated adsorption capacities obtained for the PSO model ($q_{e,cal} = 9.05$ and 17.26 for $C_i = 50, 100$ mg/L, respectively) are agree to experimental data ($q_{e,exp} = 8.97$ and 17.38 , mg/g for $C_i = 50, 100$ mg/L, respectively). As seen in Table 4, the rate constants (k_2) decrease with increasing of initial concentration confirming that the adsorption process was faster for lower initial concentration. For $C_i = 250$ mg/L, it can be seen that the nonlinear Elovich curve pass near to experimental data (Fig. 5c). Also, Elovich model gives higher value of R^2 (0.9842) compared to PFO ($R^2 = 0.7834$) and PSO ($R^2 = 0.9349$) suggesting that the adsorption process is controlled by chemisorption mechanism.

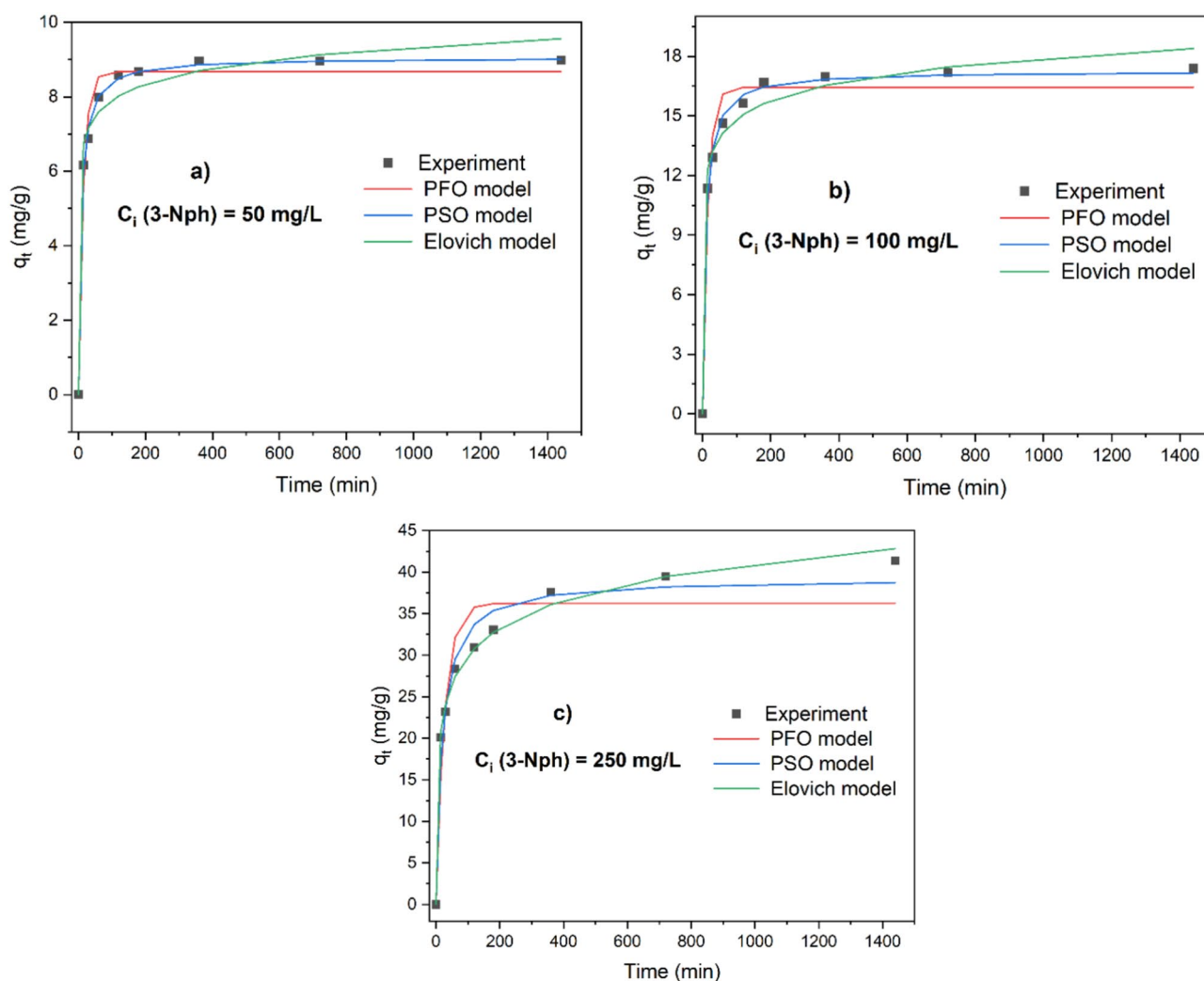


Fig. 5. Variation of adsorption capacity of MC-HC against contact time (min) at (a) $C_i = 50$ mg/L, (b) 100 mg/L and (c) 250 mg/L.

Ci (mg/L)	Pseudo-First order			Pseudo-second order			Elovich		
	q _{e,cal} (mg/g)	k ₁ ·10 ⁻² (1/min)	R ²	q _{e,cal} (mg/g)	k ₂ ·10 ⁻² g/mg.min	R ²	α g/mg.min	β (g/mg)	R ²
50	8.677	6.859	0.9043	9.054	1.417	0.9892	1.617	22.147	0.8182
100	16.443	6.398	0.8744	17.262	0.648	0.9840	0.750	1.316	0.8839
250	36.244	3.625	0.7834	39.266	0.128	0.9349	0.206	0.215	0.9842

Table 4. PFO, PSO, and Elovich kinetic parameters for different initial concentrations of 3-Nph.

Elsayed et al.⁸² developed a biocomposite aerogel (Amf-CNF/LS) and investigated its efficacy in removing methylene blue (MB), rhodamine B (RhB), and cadmium ions (Cd²⁺) from synthetic wastewater. The study specifically explored the influence of contact time and stirring speed on the adsorption process. The results showed that contact time significantly impacts the adsorption capacity, with rapid increases observed within the initial minutes of exposure, suggesting a high affinity between the aerogel and contaminants. The equilibrium was quickly reached, indicating the aerogel's efficiency in fast contaminant uptake, which is beneficial for practical wastewater treatment applications where quick removal is necessary. Stirring speed was another critical factor that influenced the adsorption efficiency. Higher stirring speeds improved the mass transfer of the adsorbate molecules to the aerogel's surface, enhancing the adsorption rate. This adjustment helped to minimize the boundary layer around the adsorbent, facilitating faster adsorbate uptake.

As shown in Table 5, the values obtained from the six error equations considered in this study (Eq X to Eq X) are minor for PSO (for Ci = 50 and 100 mg/L) than PFO and Elovich models, while for Ci = 250 mg/L, the error function values were lower for Elovich than for PFO and PSO models. This confirms the results obtained from the nonlinear of PSO, PFO and Elovich models (R²), and agree the feasibility of PSO model (for Ci = 50 and 100 mg/L) and Elovich model (for Ci = 250 mg/L).

Adsorption isotherms at different adsorbent dosage

The effect of adsorbent dosage on the adsorption capacity of 3-NpH was investigated at ambient temperature using isotherm experiments without modifying solution pH. In this study, dosages of adsorbent were 2, 4, 8 and 10 g/L, and initial concentrations of 3-NpH were varying from 25 to 1000 mg/L. Figure 6a–d show the equilibrium relationships between the 3-NpH concentrations in solution C_e(mg/L) and the adsorptive capacities at different dosages of CM-HC. It can be seen that for all adsorbent dose, the adsorption capacities of 3-NpH (q_e (mg/g)) increase with the increasing of C_e (mg/L).

The experimental adsorption isotherms data were analyzed using nonlinear equations of Langmuir, Freundlich, Temkin, and Redlich–Peterson isotherm models. Table 6 presents the isotherm parameters with adsorbent dose from 2 to 10 g/L. The results indicate that the adsorption isotherm was depended of adsorbent dosage. According to correlation coefficients showing in Table 6, Freundlich and Redlich–Peterson isotherm models were best described to the sorption data for 2 g/L of adsorbent dose, whereas, for CM-HC dosage between 4 to 10 g/L, Langmuir and Redlich–Peterson isotherm models were well to describe the adsorption process. As seen in Table 6, it was found that the Langmuir constants K_L increased from 0.309 × 10⁻² to 3.9217 × 10⁻² L/mg with increasing of adsorbent dosage from 2 to 10 g/L, which indicates the high affinity at low dosage of CM-HC. Additionally, it can be noted that the value of Freundlich constant 1/n (adsorption intensity) correspond to 2 g/L was lower compared than adsorbent dosages between 4 and 10 g/L, which means that the adsorption of 3-NpH is more favorably at lower adsorbent dosage. The Redlich–Peterson parameters presented in Table 6, show that for all values of adsorbent dosage, the exponent constant β is between 0 and 1, which indicates a good adsorption⁷⁸. In addition, for dosage 4, 8 and 10 g/L, the values of β were close to unity (β = 1.003, 0.878, and 1.0267), therefore, the Redlich–Peterson model reduces to the Langmuir model to describe the 3-NpH adsorption, whereas for dosage

Ci (mg/L)	Model	Error functions					
		ARE	SSE	Δq (%)	χ ²	EABS	RMSE
50	PFO	4.668	1.395	0.063	0.192	2.796	0.482
	PSO	1.799	0.158	0.026	0.023	0.769	0.162
	Elovich	6.743	1.456	0.070	0.183	3.198	0.493
100	PFO	6.090	7.255	0.073	0.512	7.040	1.100
	PSO	2.184	0.925	0.027	0.069	2.479	0.393
	Elovich	4.281	4.007	0.051	0.265	5.124	0.817
250	PFO	11.307	110.394	0.139	4.026	27.161	4.289
	PSO	6.036	33.167	0.080	1.249	14.123	2.351
	Elovich	2.438	6.573	0.031	0.200	5.966	1.047

Table 5. Values of error functions of PFO, PSO and Elovich kinetic models of 3-NpH (Ci = 50, 100 and 250 mg/L) on CM-HC.

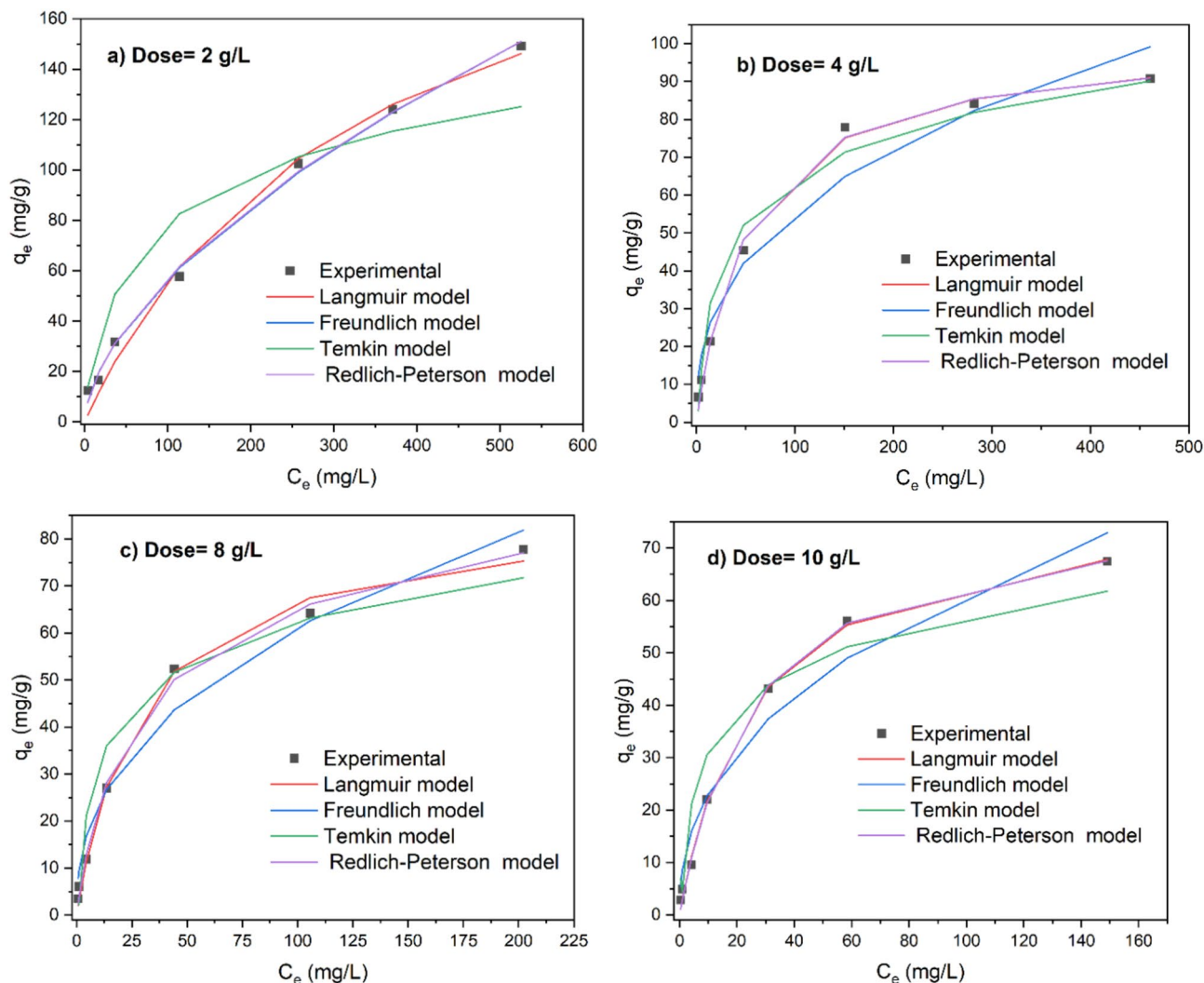


Fig. 6. Adsorption isotherms of 3-Nph on CM-HC with dosage (a) 2 g/L, (b) 4 g/L, (c) 8 g/L and (d) 10 g/L.

Isotherm Models	Parameters	Dosage (g/L)			
		2	4	8	10
Langmuir	Q_{max} (mg/g)	236.156	101.302	86.224	79.441
	K_L (L/mg) $\times 10^{-2}$	0.309	1.906	3.405	3.9217
	R^2	0.9880	0.9956	0.9945	0.9973
	n	1.689	2.639	2.415	2.357
Freundlich	K_F (mg/g)(L/mg) ^{1/n}	3.705	9.711	9.083	8.719
	R^2	0.9967	0.9547	0.9726	0.9569
Temkin	B_T (L/mg)	27.858	16.788	13.212	11.349
	A_T (KJ/mol)	0.169	0.466	1.126	1.547
	R^2	0.8624	0.9622	0.9515	0.9115
Redlich–Peterson	α_{RP} (L/mg)	4.604	0.018	0.086	0.033
	K_{RP} (L/g)	18.794	1.916	3.843	2.985
	β	0.421	1.003	0.878	1.0267
	R^2	0.9966	0.9956	0.9966	0.9974

Table 6. Langmuir and Freundlich isotherm parameters for the adsorption of 3-Nph on CM-HC at different dosages.

2 g/L, $\beta < 1$ ($\beta = 0.421$) and $\alpha_{RP} K_{RP} \gg 1$ ($\alpha_{RP} = 4.604$ and $K_{RP} = 18.794$), then the isotherm was approaching the Freundlich form, where K_{RP}/α_{RP} and $(1 - \beta)$ are related to K_F and n Freundlich parameters, respectively⁸³.

Based on the values of error functions obtained by Eqs. (7), (8), (9), (10), (11), (12), it can be observed from Table 7, that for adsorbent dosage 2 g/L, the Freundlich and Redlich–Peterson show the lowest values of APE, SSE, Δq (%), χ^2 , EABS, and RMSE. In the case of adsorbent dosages from 4 to 10 g/L, Langmuir and Redlich–Peterson present the less values of error functions compared to Freundlich and Temkin isotherm models. These results were in agreement with the finding correlation coefficients and validate the studied isotherm models.

As seen in Fig. 7a, it was found that as the amount of 3-NpH (mg/g) decrease from 236.156 to 79.441 mg/g when the adsorbent dose increases from 2 to 10 g/L. This result can be attributed to the split in the flux or the concentration gradient between solute concentration in the solution and the solute⁸⁴. Figure 7b, shows that the removal percentage of 3-NpH increase by the increasing of the sorbents dosage, this result can be attributed to the increase of the number of sorption site available, thus allow the increasing of removal percentage of 3-NpH⁸⁵.

Adsorption isotherms at different temperatures

Adsorption isotherms of 3-NpH at temperatures 300.15, 313.15 and 330.15 K on CM-HC are shown in Fig. 8a–c, respectively. It can be seen that the temperature has a significant effect on the removal of 3-NpH. As shown in these figures, it can observe that the adsorption capacity of CM-HC decreases with increasing of temperature confirming that the adsorption process of 3-NpH on CM-HC is controlled by an exothermic reaction. Previous

Dose (g/L)	Model	Error functions					
		APE	SSE	Δq (%)	χ^2	EABS	RMSE
2	Langmuir	20.157	202.234	0.331	17.856	33.444	6.360
	Freundlich	9.897	60.271	0.171	3.483	18.477	3.472
	Temkin	36.529	1712.042	0.490	24.908	95.565	18.504
	Redlich–Peterson	10.139	62.045	0.179	3.945	18.330	3.523
4	Langmuir	11.994	34.540	0.225	4.320	12.810	2.628
	Freundlich	28.452	353.942	0.429	9.463	43.842	8.414
	Temkin	21.776	216.007	0.320	9.897	32.619	6.573
	Redlich–Peterson	12.127	34.528	0.227	4.415	12.869	2.628
8	Langmuir	15.593	29.566	0.273	4.621	11.721	2.432
	Freundlich	34.850	147.949	0.584	6.908	27.085	5.440
	Temkin	27.778	218.128	0.434	13.598	30.095	6.605
	Redlich–Peterson	12.387	18.150	0.199	2.170	10.333	1.905
	Langmuir	17.941	10.984	0.313	4.535	7.285	1.482
10	Freundlich	39.794	176.909	0.582	7.917	31.924	5.948
	Temkin	48.302	285.026	0.801	12.386	36.244	7.550
	Redlich–Peterson	18.146	10.637	0.320	4.941	7.014	1.459

Table 7. Values of error functions of adsorption isotherm models of 3-NpH on CM-HC at different dosage.

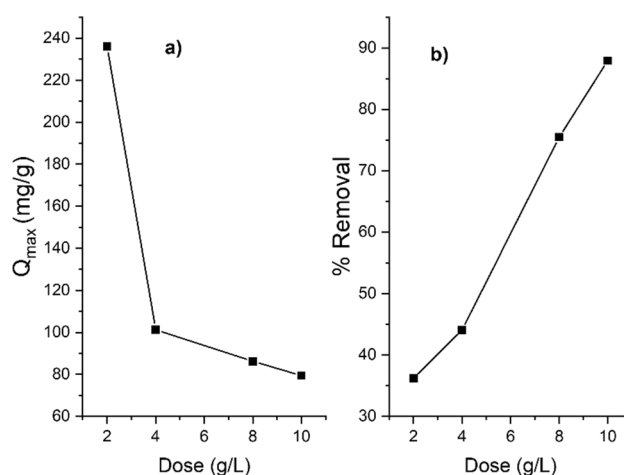


Fig. 7. Effect of sorbents dosage (g/L), on the (a) amount of 3-NpH sorbed, q_m (mg/g) and (b) percentage of 3-NpH removal; solution pH: 5.6.00; temperature: 297 K, agitation speed: 150 rpm; contact time: 24 h.

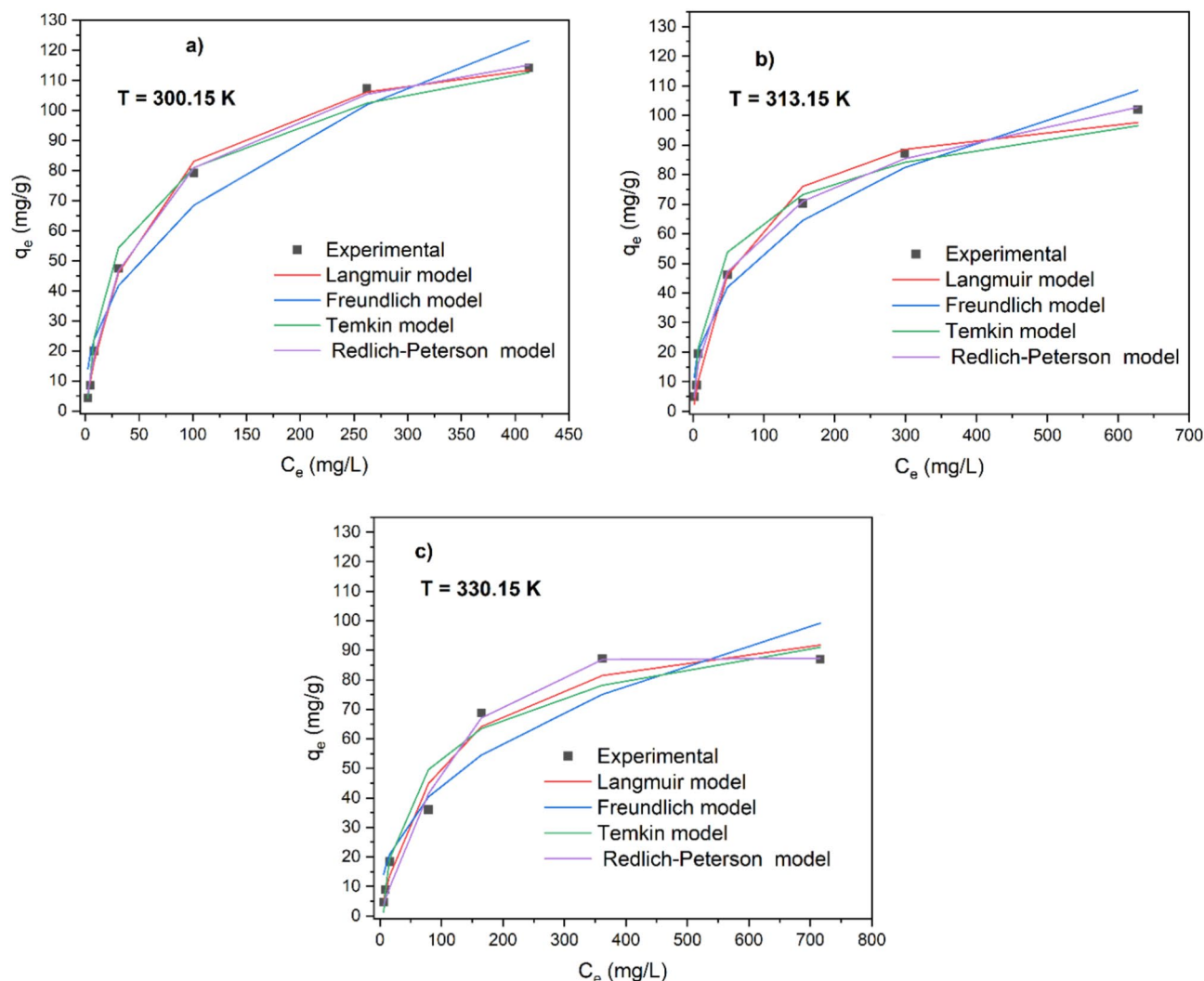


Fig. 8. Adsorption isotherms of MC-HC at temperature (a) 300.15, (b) 313.15 and (c) 330.15 K.

studies of adsorption of phenolic compounds showed an exothermic process using oil palm shell activated carbon⁸⁶, carbon black⁸⁷, cattail fiber-based activated carbon⁸⁸, and anaerobic granular sludge⁸⁹ as adsorbents. In these studies, it was suggested that the increase of temperature may cause a breaking of attraction force between the adsorbate molecules and the active sites on the surface of carbonaceous materials leading to decrease of adsorption capacity⁹⁰. The equilibrium data at temperature 300.15, 313.15 and 330.15 K were fitted using non-linear equations of Langmuir, Freundlich, Temkin and Redlich–Peterson isotherm models. Table 8 shows the isotherm parameters with their correlation coefficients R^2 . It was found that for all temperatures studied, the R^2 for Langmuir and Redlich–Peterson isotherm models are higher than Freundlich, Temkin isotherm models.

The maximum adsorption capacities of 3-Nph on CH-HC were 128.625, 107.704, and 105.441 mg/g at 300.15, 313.15 and 330.15 K, respectively. Likewise, the values of Langmuir constant K_L decrease with increasing of temperature, which indicate the higher affinity at lower temperature and confirming that the adsorption of 3-Nph is an exothermic nature. Furthermore, it can be noted that the values of parameter β are close to unity, confirming that the adsorption isotherms are best approaching to Langmuir model than Freundlich model. Table 9 presents the values of error functions. It can be observed that among four studied isotherm models, the Langmuir and Redlich–Peterson isotherm showed less values, confirming that the Langmuir model is the best fitted model for the range temperature studied.

Adsorption mechanisms

The proposed adsorption mechanisms of 3-Nph on CM-HC depended to the functional groups present on the surface on the adsorbent. In the recent study, we have found that the surface of CM-HC exhibits the following functional groups: OH, C=O, C–O, and C=C (aromatic ring)⁹¹. Therefore, electrostatic interaction can be carried out between the negative charge of OH, C=O, C–O groups with the positive charge of the nitrogen from 3-Nph. Also, the OH functional group may interact with the oxygen from phenol group by hydrogen bonding. Other interaction between the C=C group with the benzene from 3-nitrophenol by π – π interactions. Additionally,

Isotherm Models	Parameters	Temperature (K)		
		300.15	313.15	330.15
Langmuir	Q_{\max} (mg/g)	128.625	107.704	105.441
	K_L (L/mg) (10^{-2})	1.804	1.548	0.939
	R^2	0.9974	0.9842	0.9766
	N	2.393	2.698	2.455
Freundlich	K_F (mg/g)(L/mg) ^{1/n}	9.945	9.962	6.813
	R^2	0.9634	0.9742	0.9141
Temkin	B_T (L/mg)	22.475	16.664	18.761
	A_T (KJ/mol)	0.363	0.522	0.178
	R^2	0.9865	0.9744	0.9586
Redlich–Peterson	α_{RP} (L/mg)	0.035	0.123	0.0005
	K_{RP} (L/g)	2.759	3.713	0.629
	β	0.917	0.798	1.379
	R^2	0.9985	0.9971	0.9843

Table 8. Langmuir and Freundlich isotherm parameters for the adsorption of 3-Nph on CM-HC at different temperatures.

T (K)	Model	Error functions					
		APE	SSE	Δq (%)	χ^2	EABS	RMSE
300.15	Langmuir	8.279	33.754	0.118	1.274	12.653	2.598
	Freundlich	57.478	469.224	1.052	16.197	54.511	9.687
	Temkin	10.216	99.680	0.151	2.364	21.640	4.465
	Redlich–Peterson	11.258	19.641	0.187	1.190	11.190	1.982
313.15	Langmuir	18.906	144.054	0.299	11.766	24.773	5.368
	Freundlich	37.341	235.752	0.666	9.589	37.525	6.867
	Temkin	15.791	142.297	0.278	4.066	27.083	5.335
	Redlich–Peterson	9.271	26.502	0.160	1.585	11.177	2.302
330.15	Langmuir	14.555	182.855	0.182	4.808	30.997	6.047
	Freundlich	51.710	672.224	0.910	17.772	62.448	11.595
	Temkin	20.789	323.810	0.339	14.212	36.983	8.047
	Redlich–Peterson	17.807	122.489	0.272	11.221	21.007	4.950

Table 9. Values of error functions of adsorption isotherm models of 3-Nph on CM-HC at different temperatures.

CM-HC has pores that may allow the 3-Nph molecules. Figure 9 shows the electrostatic interactions, hydrogen bonding, π - π interactions, and porous adsorption as a possible adsorption mechanism of 3-Nph onto CM-HC.

Adsorption and desorption cycles

Figure 10 shows the adsorption and desorption cycles of 3-Nph onto AB-HC. It can be seen that adsorption and desorption capacities (q_{ads} and q_{des}) of 3-Nph has decreased. The decrease in adsorption capacity can be attributed to the possible remnant of 3-Nph on the surface of the CM-HC due to the strong interaction between adsorbate and adsorbent, and incomplete desorption of 3-Nph using NaOH. In other studies, moderate adsorption of nitrophenols was observed after the first cycle, which is attributed to the destruction of the porous structure of the activated biochar under alkaline experimental conditions. To improve the reusability of CM-HC, it is suggested to use other eluents or even temperature of aqueous solution.

Deep learning artificial intelligence framework to optimize the adsorption capacity of carbonaceous material

In this section, the focus centers on the implementation of a deep learning⁹² artificial intelligence (AI) algorithm utilizing an artificial neural network⁹³. Subsequently, optimization based on a genetic algorithm⁹⁴ is applied. This comprehensive procedure is executed methodically, with the initial step encompassing data visualization and description, followed by AI implementation and optimization.

Data visualization and description

Regarding data visualization and description, the entire experimental dataset is initially formatted and consolidated into a structure, as illustrated in Table 10⁹⁵. Each column in this table contains variables such as time, initial

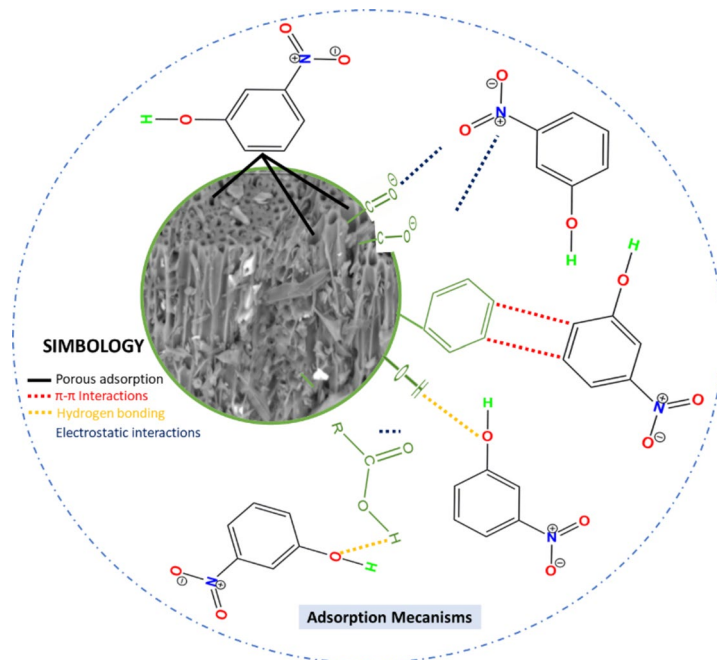


Fig. 9. Adsorption mechanism of 3-Nph on CM-HC.

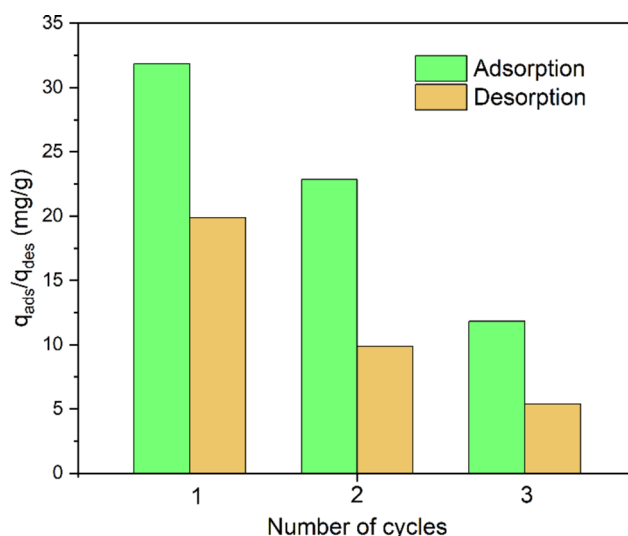


Fig. 10. Adsorption and desorption cycles of 3-Nph on CM-HC.

concentration, pH, dosage, temperature, and the fitness function (removal percentage). Each row corresponds to an individual experimental run, mirroring the real experimental procedure, which can be resource-intensive. For instance, the execution of experiment run no. 8 required 1440 min. Despite the substantial time investment, consolidating the database at this juncture proves beneficial.

To elucidate the data description, violin plots (Fig. 11) are employed for each of the five variables and the removal percentage, the latter being the fitness function. The violin plot is chosen for its ability to convey data properties akin to a box and whisker plot, while also providing insights into data distribution. An alternative method for understanding data distribution is through histograms, as depicted in the scatter matrix of Fig. 12.

The violin plot reveals distinctive patterns, such as a concentration of the time variable towards the upper end, aligning with the scatter matrix histogram. Furthermore, there is a noticeable concentration at the lower end, indicating durations less than 200 min. Notably, there is an abundance of experimentation for lower initial concentrations (< 200 units), a trend consistent with the scatter matrix results showcasing the highest data density in this range.

Experimental run no.	Time	Initial concentration	pH	Dosis	temperature	Removal percentage
1	15	50	6	1	300.15	47.04
2	30	50	6	1	300.15	61.87
3	60	50	6	1	300.15	68.96
4	120	50	6	1	300.15	80.01
5	180	50	6	1	300.15	86.09
6	360	50	6	1	300.15	86.94
7	720	50	6	1	300.15	89.74
8	1440	50	6	1	300.15	91.06
.
.
.
.
82	1440	50	6	1	330.15	83.71
83	1440	100	6	1	330.15	85.46
84	1440	250	6	1	330.15	69.56
85	1440	500	6	1	330.15	67.60
87	1440	700	6	1	330.15	54.67
87	1440	1000	6	1	330.15	37.78

Table 10. General format of the experimental data. Data publicly available at: <https://dx.doi.org/10.6084/m9.figshare.24545587>.

The pH variable exhibits its highest density just below the neutral point, with bottlenecks observed around pH values of 4–5 and 7. This aligns with the scatter matrix, emphasizing lower probability density at the ends compared to a peak at 6. The dosage and temperature graphs share a similar pattern, with higher probability distribution for lower dosages (< 2 units) and temperatures (< 305 K). However, as dosages and temperatures increase, the number of data points decreases.

The removal percentage's violin plot correlates intriguingly with the histogram distribution in the scatter matrix. The highest frequency of removal percentage occurs at approximately 90 units, with a noticeable reduction in data points beyond this threshold. The upper end of the 90-unit range exhibits a more substantial data distribution compared to the lower end, suggesting a potential combination of the five design variables yielding maximum removal percentage.

It should be noted that the dataset used for the ANN analysis comprises 87 entries, which may be considered small for robust ANN applications. This limitation could potentially affect the generalizability of the model. To address this issue in future studies, we propose to expand the dataset through additional batch experiments to enhance the training process and improve the model's accuracy and generalizability. Further, employing cross-validation methods or increasing the diversity of the data points could also contribute to more reliable ANN predictions. These steps will help in mitigating the effects of the current dataset size and provide a more robust framework for ANN applications in adsorption batch experiments.

In this phase, correlation heat maps incorporating coefficients from Pearson⁹⁶, Spearman⁹⁷, and Kendall⁹⁸ methods have been successfully implemented and are visually represented in Fig. 13. Notably, all three heat maps exhibit a correlation coefficient of 1 along the diagonal, indicating pairwise correlations such as time-time, initial concentration with initial concentration, among others. Conversely, the data situated above or below the diagonal represents a mirrored image. Consequently, it is appropriate to focus solely on interpreting one side of the correlation heat map. The primary emphasis of this discussion is on the significance of the correlation coefficient values and the distinctions arising from the implementation of different correlation methods. It is imperative to acknowledge that, in all instances, a positively correlated coefficient is exclusively observed for time and dosage, with Pearson correlation coefficients of 0.26 and 0.38, respectively. It can be asserted that the relationship between time and the removal percentage does not exhibit a strongly positive correlation; however, dosage demonstrates a more robust positive correlation with a coefficient of 0.38. Nonetheless, this interpretation undergoes notable variations when examining the Kendall correlation, which implies that time possesses a more potent correlation coefficient with the removal percentage compared to dosage—an observation similarly noted with the Spearman method. This leads to the conclusion that the determination of whether time or dosage more significantly influences the removal percentage is inconclusive. Nevertheless, all three algorithms consistently affirm the existence of a positive relationship. The correlation coefficient of pH, as determined by all three methods, is negative. However, its value is in close proximity to zero, signifying that pH is not the most robust or influential variable affecting the removal percentage. A parallel trend is observed for temperature, displaying a negative correlation coefficient, suggesting that lower temperatures are preferable for achieving higher removal percentages. The most substantial correlation is identified for the initial concentration concerning the removal percentage, with values of -0.59 for both Pearson and Spearman correlations, and -0.45 for the Kendall correlation. This indicates that the initial concentration emerges as the most influential parameter for the removal percentage, with lower initial concentrations proving more conducive to achieving favorable outcomes.

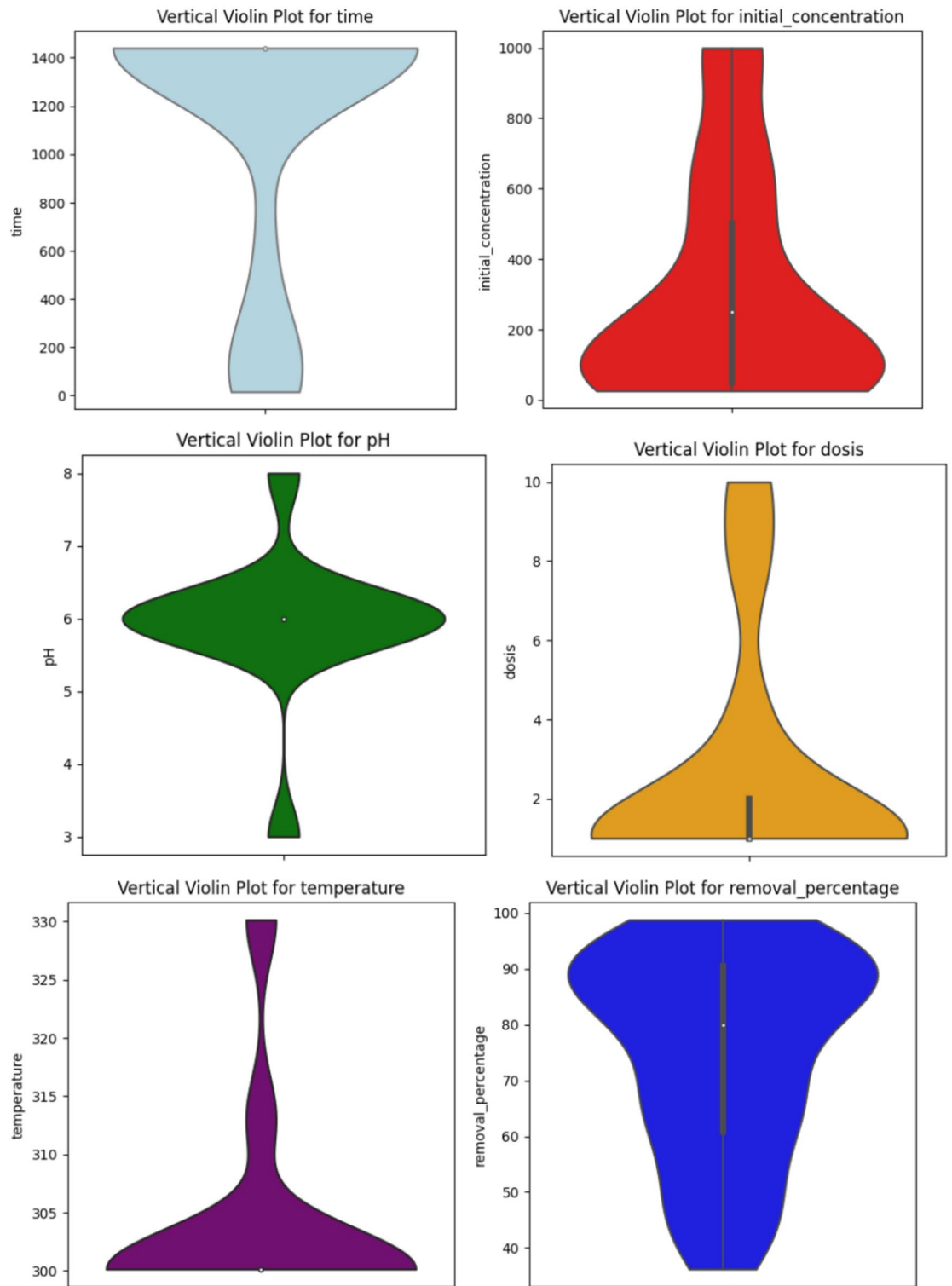


Fig. 11. Violin plot of the variables and the fitness function.

Deep learning artificial neural network

For enhanced accuracy and mitigating multicollinearity issues within the dataset, an advanced approach involving deep learning artificial neural networks (ANNs)⁹⁹ was implemented for deep learning purposes^{100,101}. Previous attempts using traditional machine learning techniques such as multivariate regression analysis and support vector machine yielded unsatisfactory results, prompting the adoption of ANNs.

The initial ANN configuration consisted of a single hidden layer comprising 10 neurons. Architecture optimization was pursued by employing the Adam¹⁰² optimizer in Python¹⁰³, within the Google Colab environment¹⁰⁴.

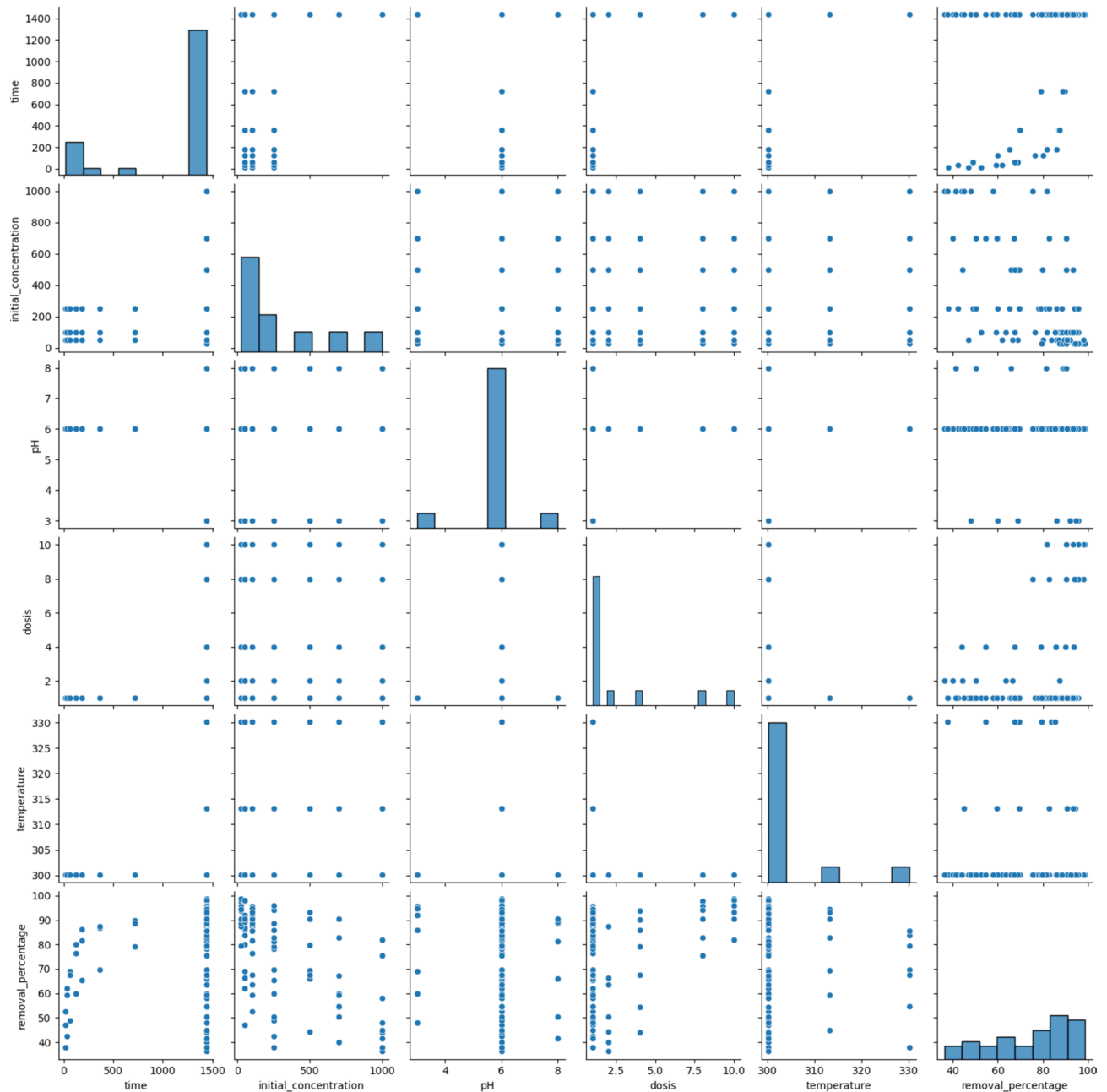


Fig. 12. Scatter matrix with histograms between the design variables and the fitness function.

Despite multiple iterations, the mean square error (MSE)¹⁰⁵ ranged between 75.8409 and 156.8976, indicating suboptimal performance.

To address this, manual iterations were conducted by varying the number of hidden layers and neurons, transitioning from a structure of 5-10-10-1 to 5-100-100-1. Unfortunately, this did not yield satisfactory results. The implementation was then transferred to MATLAB¹⁰⁶, where the scaled conjugate method¹⁰⁷, known for its suitability in regression fits for small and noisy datasets, was adopted.

The optimized architecture identified was 5-14-14-1 (refer to Fig. 14). This architecture includes an input layer with five variables, two hidden layers with 14 neurons each utilizing a *tansig* activation function, and an output layer representing the removal percentage with a linear activation function.

The *Tansig* function, or hyperbolic tangent sigmoid transfer function, is a popular activation function used in neural networks, particularly in the context of artificial neural networks (ANNs). Mathematically, it is defined as: $tansig(x) = \frac{2}{1+e^{-2x}} - 1$, where x represents the input to the function. This function outputs values that range from -1 to 1 , making it particularly useful for modeling data that have been normalized to this range. The *Tansig* function is an S-shaped curve, similar to the logistic sigmoid function, but with outputs spread over a wider range on the y-axis. This characteristic allows the function to handle negative values more naturally and makes it beneficial for problems where the symmetry around zero can help in faster convergence of the learning

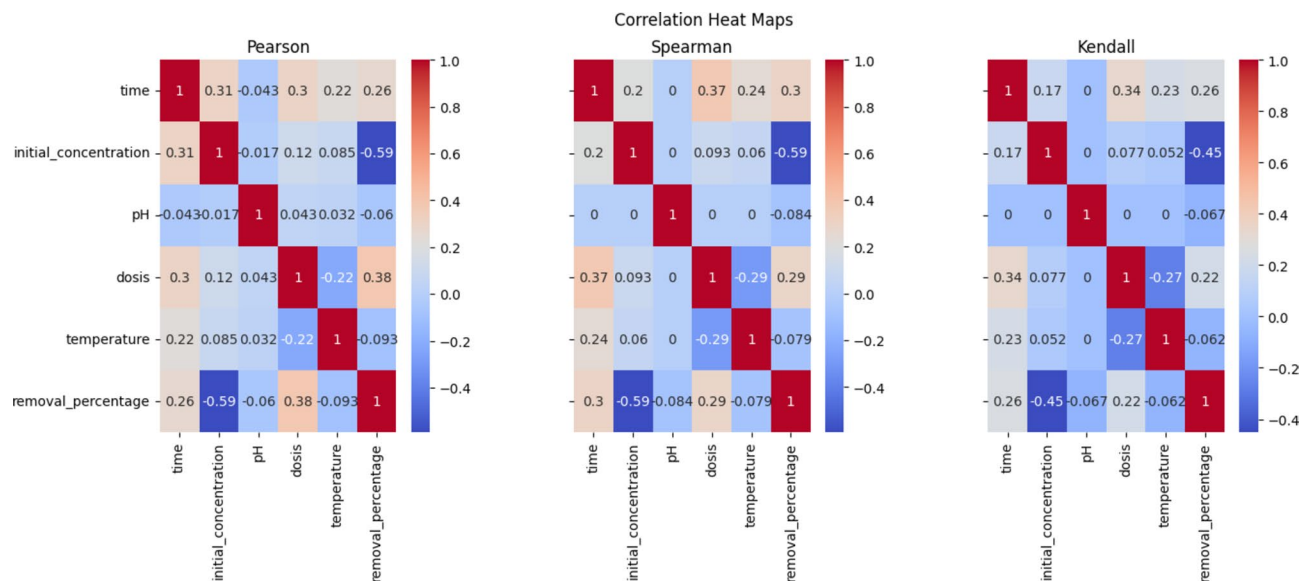


Fig. 13. Coefficient of correlation of Pearson, Spearman, and Kendall.

algorithm. The use of the *Tansig* function in neural networks is advantageous because of its non-linear nature, which enables the network to learn complex patterns that linear models might not be able to capture. Additionally, the gradients of the *Tansig* function are stronger for values in the range closer to zero, which can lead to more effective and efficient training phases, especially during backpropagation where gradients are used to update the weights. In the context of our ANN model used to analyze adsorption batch experiments, employing the *Tansig* function as the activation helps the network in handling varying dynamics of the data while maintaining stable learning and convergence behaviors. This choice is crucial for the performance of our ANN, particularly given the constraints imposed by the relatively small size of the dataset.

The iterative adjustment of bias and weight matrices in each epoch led to the optimal values at Epoch 228 (see Fig. 15), resulting in MSE values of 4.07, 18.406, and 6.2122 for the training, testing, and total datasets, respectively (refer to Table 11).

The coefficient of determination, corresponding to R-squared values, for training, testing, and the total dataset were 0.98759, 0.94280, and 0.98108, respectively. This confirmed the efficacy of the selected architecture and convergence criteria. The output generated from this optimized model was saved for further analysis and interpretation.

Upon establishing the architecture and statistical characteristics of the proposed artificial neural network (ANN) model, the subsequent phase involves a comprehensive graphical visualization to assess the model's performance. While statistical indicators provide crucial insights, graphical representations offer additional nuances that may not be discernible through numerical metrics alone.

In Fig. 16a, the regression fit graph portrays the relationship between the target variable (experimental removal percentage) and the model's output (simulated removal percentage). Ideally, a perfect linear correlation between these variables signifies an impeccable goodness of fit. The linear fit equation reveals a slope of 1.00, indicating a consistent rate of change between the target and output. However, a bias of -0.56 is observed, implying a slight deviation of the y-intercept from the origin, a phenomenon rationalized by the scarcity of data points below a removal percentage of 50. Notably, the graph includes representations of both training and testing data. Strikingly, the statistical performance of the training dataset aligns more closely with the linear regression line than the testing data. Instances of substantial deviation from the regression line in the testing data caution against over-reliance on this subset for optimization, as poorly predicted points may lead to local optima⁴⁷.

Furthermore, adherence to key regression assumptions is imperative for robust model validation¹⁰⁸. Figure 16b delves into the examination of normality, independence, and homoscedasticity of errors. The normality of errors is scrutinized using a QQ-plot, where the majority of data points closely adhere to the theoretical normal distribution line. However, six outlier data points, positioned at the extremes of the distribution, warrant careful consideration during the optimization phase. Independence of errors is assessed through a plot of residuals against experimental run (row number). The absence of a discernible pattern in this plot affirms the independence of errors. Intriguingly, the same six outlier data points identified earlier exhibit distinctive characteristics, emphasizing the need for meticulous handling during optimization. Finally, homoscedasticity of residuals is validated via a plot correlating predicted values with residuals. The absence of a defined pattern in this plot further confirms the homogeneity of residuals. Notably, the six outlier points exhibit unique behaviors in this context as well, underscoring their significance in the overall analysis.

In conclusion, this multifaceted graphical analysis provides a comprehensive evaluation of the ANN model's performance, ensuring a thorough understanding of its strengths and potential limitations in addressing the research objectives.

The validation of our deep learning artificial neural network (ANN) is a critical step to ensure the reliability and accuracy of the model's predictive capabilities. We employed a robust validation strategy that involves

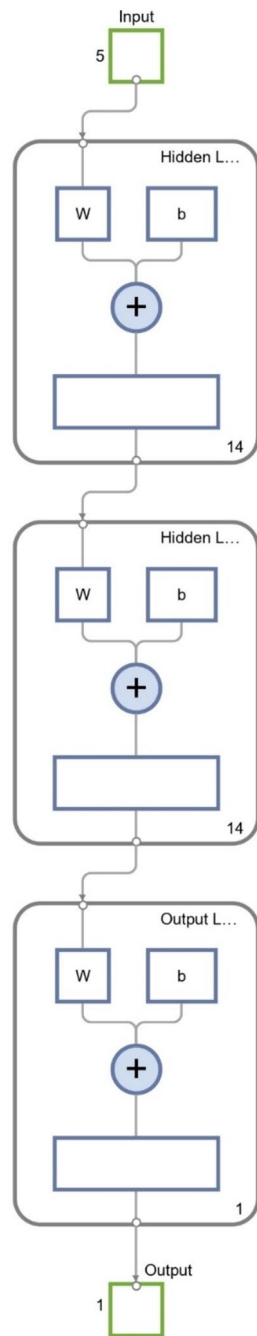


Fig. 14. Optimal deep learning architecture.

splitting the data into distinct sets: training, testing, and validation. This separation ensures that the model is not only trained but also fine-tuned and tested against unseen data. During the training phase, the model's parameters are adjusted to minimize the error on the training set. Then, the validation set is used to tune the hyperparameters and prevent the model from overfitting, which is critical given the relatively small dataset. The final model's performance is assessed on a separate test set, which provides an unbiased evaluation of its predictive power. The mean square error (MSE) and the coefficient of determination (R^2) are calculated for each set to quantify the model's accuracy and predictive performance. These metrics confirm whether the model can effectively generalize beyond the training data.

Ensuring the repeatability of our ANN model involves detailed documentation of the model architecture, including the number of layers, the type of activation functions used (e.g., *Tansig*), and the optimization algorithms (e.g., scaled conjugate method). The iterative process of model training is set to reproducible conditions, with fixed seeds for random number generators and consistent training-validation-test splits. This practice is vital to achieve consistent results when the model is re-run under the same conditions or by other researchers. Additionally, the robustness of the model is tested through repeated runs, where the stability of the results (such

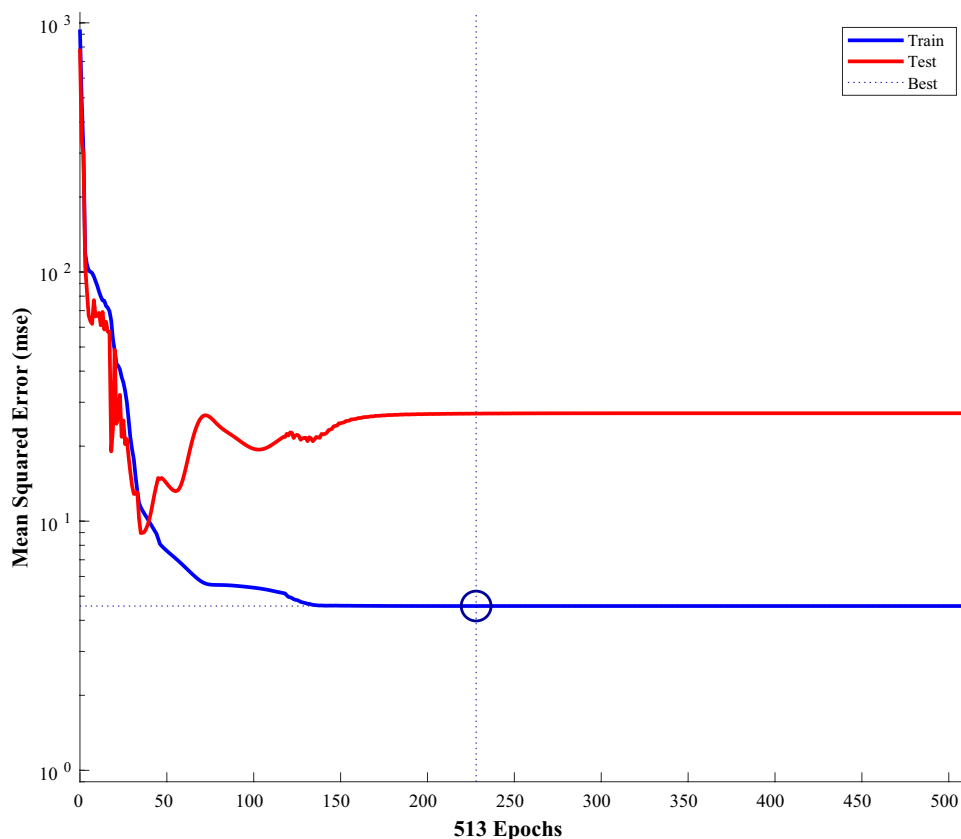


Fig. 15. Convergence criteria of the Mean Squared Error for the best architecture.

Source	MSE	MAPE	SSE	R ²
Training	4.07	1.7369	301.18	0.98759
Testing	18.406	4.9067	239.28	0.94280
Total	6.2122	2.2105	540.46	0.98108

Table 11. Statistical performance indicators for the best architecture.

as MSE and R² values) is checked across different iterations to ensure that the outcomes are not anomalies but reproducible findings.

Optimization using genetic algorithm

The employment of deep learning has facilitated the establishment of an empirical correlation between various tuning parameters and the fitness function, represented by the removal percentage. This correlation serves as a fitness function equation, enabling the formulation of an optimization problem. The objective of this optimization is to maximize the removal percentage by adjusting decision variables such as time, initial concentration, pH, dosis, and temperature. The decision variable bounds are defined as lower bound = [15, 50, 3, 1, 300.15] and upper bound = [1440, 250, 8, 10, 330.15]. To conform to typical optimization conventions geared towards minimization, the removal percentage is multiplied by -1 . A noteworthy concern arises from the lack of a continuous dataset for digital twin modeling. Despite the high performance demonstrated during empirical modeling, the optimization process operates with a potential error margin due to the finite nature of the removal percentage (with a maximum value of 100).

The optimization problem is expressed as follows:

$$\begin{aligned} \text{Minimize : } & -1 \times \text{removal percentage subject to lower bound} \\ & \leq [\text{time, initial concentration, pH, dosis, temperature}] \\ & \leq \text{upper bound } 0 \leq \text{removal percentage} \leq 100. \end{aligned}$$

Prior to mathematical optimization, a critical step involves visualizing the optimization data to identify potential regions for improvement. Given the multivariate nature of the data (six dimensions), a parallel coordinate

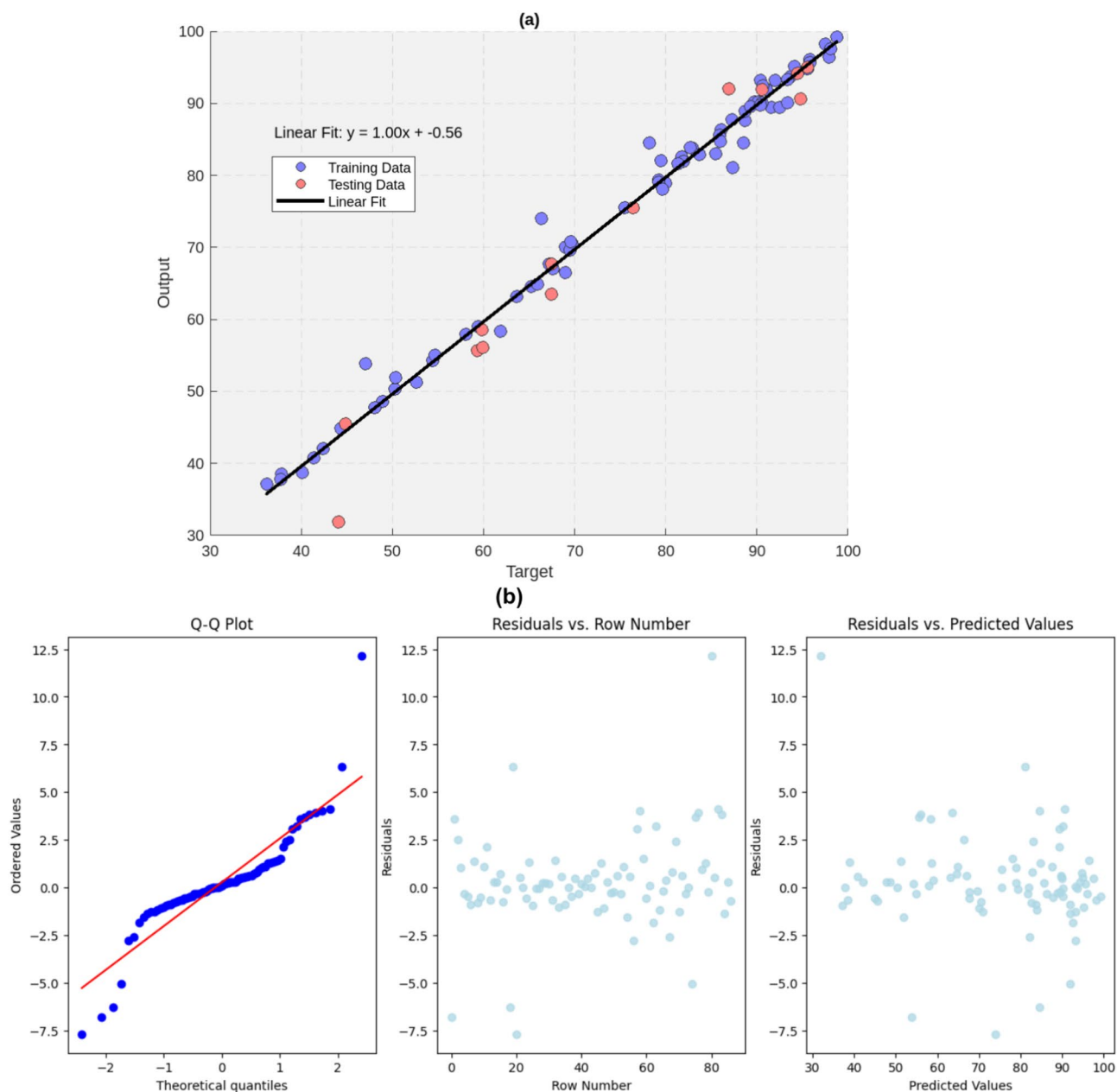


Fig. 16. (a) Regression fitting for the optimal architecture. (b) Verification of the assumptions of the regression fit, including normality, independence, and homoscedasticity from left to right.

plot is adopted (Fig. 17). In this plot, red lines signify a higher tendency for improved removal percentage. Analysis of the red lines indicates that lower temperatures, reduced dosis, moderate pH values, moderate initial concentration, and extended time are favorable for optimization. However, a formal algorithmic application is required to substantiate these observations.

To address this, a single-objective genetic algorithm¹⁰⁹ implemented in MATLAB, utilizing the ‘ga’ function, is employed for optimization. The chosen parameters include a population size of 50, a maximum of 100 generations, and parallel computing. The results of this optimization process are tabulated in Table 12.

In Table 12, simulation results stemming from data-driven optimization through a deep learning algorithm are presented. Notably, the simulated maximum removal percentage reaches 100.001, a theoretically ideal value with a tolerance level of 0.001. While this represents an idealized outcome, the simulation aids in identifying decision variable combinations leading to this optimality. However, acknowledging the inherent error margin in the digital twin modeling and optimization process, it is crucial to validate the true optimality through experimentation.

A subsequent experiment, conducted under conditions aligning with the optimal points identified in simulation, yields a removal percentage of 98.77%. The percentage difference between this experimentally verified optimality and the simulated result is a mere 1.24%, demonstrating the success of applying deep learning with

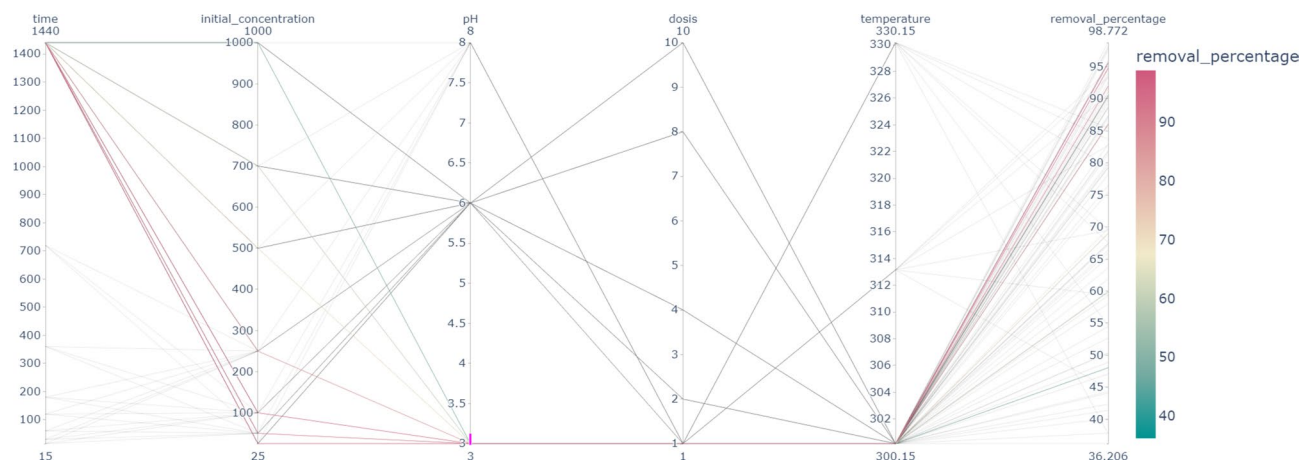


Fig. 17. Parallel coordinate plot.

Source	Time	Initial concentration	pH	Dosis	Temperature	Removal percentage
Simulation	1381.2912	23.0771	5.7939	9.1888	305.6714	100.001
Experimentation	1440	25	6	10	300.15	98.77

Table 12. Optimality based upon simulation and experimentation.

genetic algorithm optimization. Consequently, it is recommended to prioritize experimental optimality for robust validation.

Conclusion

It is concluded that the carbonaceous material from *Haematoxylum campechianum* waste (CM-CM) proved to be an effective low-cost adsorbent to remove 3-nitrophenol from aqueous solution. The experiment results show that the uptake capacity of 3-Nph by CM-HC is dependent of contact time, pH of solution, adsorbent dosage and temperature parameters. Removal of 3-Nph was found to be more favorable at pH = 6 and at T = 300.15 K. Over concentrations studied, adsorption equilibrium data showed the best fitted Langmuir model at all pH solutions, dosage of adsorbent and temperatures studied. The maximum adsorption capacity of CM-HC was calculated as 236.156 mg/g. The results of kinetic study show that for C_i (3-Nph) = 50–100 mg/L, the pseudo-second order model was best fit model to the adsorption of 3-Nph. Some other conclusions from the data analytics are following:

1. The relationship between time, dosage, and various environmental factors with the removal percentage is explored through correlation analysis using Pearson, Spearman, and Kendall methods. Despite differences in the strength of correlations between the methods, a consistent positive correlation exists between time and dosage with the removal percentage. The interpretation varies slightly among methods, highlighting the nuanced influence of correlation algorithms. Notably, the initial concentration emerges as the most influential parameter, emphasizing its significance in achieving favorable outcomes. The study suggests that determining whether time or dosage more significantly influences the removal percentage remains inconclusive, but the positive relationship is consistently affirmed by all three correlation algorithms.
2. The identified 5-14-14-1 architecture, fine-tuned over 228 epochs, demonstrated robust performance with mean squared error (MSE) values of 4.07, 18.406, and 6.2122 for training, testing, and total datasets, respectively. The coefficient of determination (R-squared) values further confirmed the efficacy of the selected architecture. The graphical analysis of the model's performance revealed a well-fitted linear correlation between experimental and simulated removal percentages, with attention to potential pitfalls in relying solely on the testing dataset for optimization. The assessment of normality, independence, and homoscedasticity of errors provided a comprehensive understanding of the model's strengths and limitations.
3. Through the approach of a single-objective genetic algorithm implemented in MATLAB, a theoretically ideal removal percentage of 100.001 was simulated, aiding in identifying decision variable combinations leading to optimality. The subsequent experimental validation under optimal conditions yielded a removal percentage of 98.77%, showcasing the success of combining deep learning with genetic algorithm optimization. However, it is emphasized that experimental validation is crucial to account for inherent error margins in digital twin modeling. The study recommends prioritizing experimental optimality for robust validation of the optimization results obtained through the integration of deep learning and genetic algorithms.

This research not only contributes to the advancement of environmental science but also offers a unique opportunity for educational innovation. By incorporating artificial neural networks, deep learning, and data science methodologies into the study of adsorption processes for pollutant removal, students can engage in cutting-edge interdisciplinary approaches. The utilization of genetic algorithm optimization adds a practical dimension to their learning experience, fostering skills in optimization and critical thinking. This innovative integration of advanced technologies provides students with valuable exposure to real-world problem-solving, preparing them for future challenges in environmental engineering and promoting a forward-looking educational model.

Overall, the combination of using biosorbents for environmental remediation and enhancing these efforts through educational programs presents a holistic approach to managing water pollution. The research underscores the importance of continuous research in biosorbent efficacy and advocates for robust educational programs that empower individuals with the knowledge and skills to make impactful environmental decisions. Future strategies should focus on expanding the availability of educational resources related to biosorbents and increasing public engagement through tailored educational programs that highlight the practical aspects of environmental stewardship (Supplementary Information).

Data availability

The datasets generated and analysed during the current study are available in the figshare repository, [<https://dx.doi.org/10.6084/m9.figshare.24545587>].

Received: 2 March 2024; Accepted: 22 August 2024

Published online: 30 August 2024

References

- Sharma, N., Paço, A. & Upadhyay, D. Option or necessity: Role of environmental education as transformative change agent. *Eval. Progr. Plan.* **97**, 102244 (2023).
- Díaz-López, C. *et al.* Sensitivity analysis of trends in environmental education in schools and its implications in the built environment. *Environ. Dev.* **45**, 100795 (2023).
- Kroufek, R., Cincera, J., Kolenaty, M., Zalesak, J. & Johnson, B. “I had a spider in my mouth”: What makes students happy in outdoor environmental education programs. *Eval. Progr. Plan.* **99**, 102326 (2023).
- Xie, Y., Chen, Z., Tang, H., Boadu, F. & Yang, Y. Effects of executives’ pro-environmental education and knowledge sharing activities on eco-friendly agricultural production: Evidence from China. *J. Clean. Prod.* **395**, 136469 (2023).
- Arora, P. K., Srivastava, A. & Singh, V. P. Bacterial degradation of nitrophenols and their derivatives. *J. Hazard. Mater.* **266**, 42–59 (2014).
- Xiong, Z., Zhang, H., Zhang, W., Lai, B. & Yao, G. Removal of nitrophenols and their derivatives by chemical redox: A review. *Chem. Eng. J.* **359**, 13–31 (2019).
- Uberoi, V. & Bhattacharya, S. K. Toxicity and degradability of nitrophenols in anaerobic systems. *Water Environ. Res.* **69**, 146–156 (1997).
- Kidak, R. & Ince, N. H. Ultrasonic destruction of phenol and substituted phenols: A review of current research. *Ultrason. Sonochem.* **13**, 195–199 (2006).
- Moraes, F. C., Tanimoto, S. T., Salazar-Banda, G. R., Machado, S. A. S. & Mascaro, L. H. A new indirect electroanalytical method to monitor the contamination of natural waters with 4-nitrophenol using multiwall carbon nanotubes. *Electroanalysis* **21**, 1091–1098 (2009).
- Guidelines for drinking-water quality: fourth edition incorporating the first and second addenda. Geneva: World Health Organization. Licence: CC BY-NC-SA 3.0 IGO. <https://iris.who.int/bitstream/handle/10665/352532/9789240045064-eng.pdf?sequence=1>. Accessed 29 Aug 2024 (2022).
- DIRECTIVE 2008/105/EC OF THE EUROPEAN PARLIAMENT AND OF THE COUNCIL of 16 December 2008 on environmental quality standards in the field of water policy, amending and subsequently repealing Council Directives 82/176/EEC, 83/513/EEC, 84/156/EEC, 84/491/EEC, 86/280/EEC and amending Directive 2000/60/EC of the European Parliament and of the Council. <https://eur-lex.europa.eu/legal-content/EN/TXT/PDF/?uri=CELEX:32008L0105>. <https://eur-lex.europa.eu/legal-content/EN/TXT/PDF/?uri=CELEX:32008L0105>. Accessed 29 Aug 2024 (2008).
- [In Spanish] NORMA Oficial Mexicana NOM-127-SSA1-2021, Agua para uso y consumo humano. Límites permisibles de la calidad del agua. <https://agua.org.mx/wp-content/uploads/2022/05/DOF-%E2%80%93Norma-Oficial-Mexicana-NOM-127-SSA1-2021-SEGOB.pdf>. <https://agua.org.mx/wp-content/uploads/2022/05/DOF-%E2%80%93Norma-Oficial-Mexicana-NOM-127-SSA1-2021-SEGOB.pdf>. Accessed 29 Aug 2024 (2022).
- Preiss, A. *et al.* Advanced high-performance liquid chromatography method for highly polar nitroaromatic compounds in ground water samples from ammunition waste sites. *J. Chromatogr. A* **1216**, 4968–4975 (2009).
- Asman, W. A. H. *et al.* Wet deposition of pesticides and nitrophenols at two sites in Denmark: Measurements and contributions from regional sources. *Chemosphere* **59**, 1023–1031 (2005).
- Belloli, R. *et al.* Nitrophenols in air and rainwater. *Environ. Eng. Sci.* **23**, 405–415 (2006).
- Schwarzbauer, J., Ricking, M. & Littke, R. Quantitation of nonextractable anthropogenic contaminants released from Teltow Canal sediments after chemical degradation. *Acta. Hydrochim. Hydrobiol.* **31**, 469–481 (2004).
- Harrison, M. A. J. *et al.* Nitrated phenols in the atmosphere: A review. *Atmos. Environ.* **39**, 231–248 (2005).
- Sarkar, S. K. *et al.* Water quality management in the lower stretch of the river Ganges, east coast of India: An approach through environmental education. *J. Clean. Prod.* **15**, 1559–1567 (2007).
- Tebbutt, T. H. Y. & Woods, D. R. A new approach to education and training in water and environmental management. *Water Sci. Technol.* **38**, 261–269 (1998).
- Papavasileiou, H. & Mavrakis, A. Environmental education: Issue water: Different approaches in secondary general and technical lyceum in a social and environmental stressed area in Greece. *Procedia Technol.* **8**, 171–174 (2013).
- Mariolakos, I., Kranioti, A., Markatselis, E. & Papageorgiou, M. Water, mythology and environmental education. *Desalination* **213**, 141–146 (2007).
- Gebrekidan, T. K. Environmental education in Ethiopia: History, mainstreaming in curriculum, governmental structure, and its effectiveness: A systematic review. *Heliyon* **10**, e30573 (2024).
- Raza, W. *et al.* Removal of phenolic compounds from industrial waste water based on membrane-based technologies. *J. Ind. Eng. Chem.* **71**, 1–18 (2019).
- Mohamad Said, K. A., Ismail, A. F., Abdul Karim, Z., Abdullah, M. S. & Hafeez, A. A review of technologies for the phenolic compounds recovery and phenol removal from wastewater. *Process Saf. Environ. Prot.* **151**(257), 289 (2021).

25. Ahmaruzzaman, Md. Adsorption of phenolic compounds on low-cost adsorbents: A review. *Adv. Colloid Interface Sci.* **143**, 48–67 (2008).
26. Nafees, M. & Waseem, A. Organoclays as sorbent material for phenolic compounds: A review. *Clean* **42**, 1500–1508 (2014).
27. Bo, L., Chen, S., Quan, X., Liu, X. & Zhao, H. Microwave assisted wet oxidation of p-nitrophenol. *Sci. China Ser. E Technol. Sci.* **48**, 220–232 (2005).
28. Kasture, N. S. Bioremediation of nitroaromatics: An overview. *Int. J. Environ. Agric. Biotechnol.* **2**, 2715–2719 (2017).
29. Bazrafshan, E., Mostafapour, F. K. & Mansourian, H. J. Phenolic compounds: Health effects and its removal from aqueous environments by low cost adsorbents. *Health Scope* **2**, 65–66 (2013).
30. Tran, V. S. *et al.* Typical low cost biosorbents for adsorptive removal of specific organic pollutants from water. *Bioresour. Technol.* **182**, 353–363 (2015).
31. Banat, F. A., Al-Bashir, B., Al-Asheh, S. & Hayajneh, O. Adsorption of phenol by bentonite. *Environ. Pollut.* **107**, 391–398 (2000).
32. Kuleyin, A. Removal of phenol and 4-chlorophenol by surfactant-modified natural zeolite. *J. Hazard. Mater.* **144**, 307–315 (2007).
33. Abatal, M. & Olguin, M. T. Comparative adsorption behavior between phenol and p-nitrophenol by Na- and HDTMA-clinoptilolite-rich tuff. *Environ. Earth Sci.* **69**(2691), 2698 (2013).
34. Phan, T. N. T., Bacquet, M. & Morcellet, M. Synthesis and characterization of silica gels functionalized with monochlorotriazinyl β -cyclodextrin and their sorption capacities towards organic compounds. *J. Incl. Phenom.* **38**, 345–359 (2000).
35. Wang, S. & Peng, Y. Natural zeolites as effective adsorbents in water and wastewater treatment. *Chem. Eng. J.* **156**, 11–24 (2010).
36. Li, Y. *et al.* Adsorption behavior of phenol by reversible surfactant-modified montmorillonite: Mechanism, thermodynamics, and regeneration. *Chem. Eng. J.* **334**, 1214–1221 (2018).
37. Alkaram, U. F., Mukhlis, A. A. & Al-dujaili, A. H. The removal of phenol from aqueous solutions by adsorption using surfactant-modified bentonite and kaolinite. *J. Hazard. Mater.* **169**, 324–332 (2009).
38. Wu, J. & Yu, H. Q. Biosorption of 2,4-dichlorophenol from aqueous solution by *Phanerochaete chrysosporium* biomass: Isotherms, kinetics and thermodynamics. *J. Hazard. Mater.* **137**, 498–508 (2006).
39. Denizli, A., Cihangir, N., Tüzmen, N. & Alsancak, G. Removal of chlorophenols from aquatic systems using the dried and dead fungus *Pleurotus sajor caju*. *Bioresour. Technol.* **96**, 59–62 (2005).
40. Colella, L. S., Armenante, P. M., Kafkewitz, D., Allen, S. J. & Balasundaram, V. Adsorption isotherms for chlorinated phenols on activated carbons. *J. Chem. Eng. Data* **43**, 573–579 (1998).
41. Caturla, F., Martín-Martínez, J. M., Molina-Sabio, M., Rodríguez-Reinos, F. & Torregrosa, R. Adsorption of substituted phenols on activated carbon. *J. Colloid Interface Sci.* **124**, 528–534 (1988).
42. Daifullah, A. A. M. & Girgis, B. S. Removal of some substituted phenols by activated carbon obtained from agricultural waste. *Water Res.* **32**, 1169–1177 (1998).
43. Rengaraj, S., Moon, S. H., Sivabalan, R., Arabindoo, B. & Murugesan, V. Agricultural solid waste for the removal of organics: Adsorption of phenol from water and wastewater by palm seed coat activated carbon. *Waste Manag.* **22**, 543–548 (2002).
44. Tariq, R. *et al.* Artificial intelligence assisted technoeconomic optimization scenarios of hybrid energy systems for water management of an isolated community. *Sustain. Energy Technol. Assess.* **48**, 101561 (2021).
45. Tariq, R. *et al.* Digital twin models for optimization and global projection of building-integrated solar chimney. *Build. Environ.* <https://doi.org/10.1016/j.buildenv.2022.108807> (2022).
46. Tariq, R. *et al.* Data engineering for digital twinning and optimization of naturally ventilated solar façade with phase changing material under global projection scenarios. *Renew. Energy* **187**, 1184–1203 (2022).
47. Tariq, R., Abatal, M. & Bassam, A. Computational intelligence for empirical modeling and optimization of methylene blue adsorption phenomena using available local zeolites and clay of Morocco. *J. Clean. Prod.* **370**, 133517 (2022).
48. Khanmohammadi, S., Musharavati, F. & Tariq, R. A framework of data modeling and artificial intelligence for environmental-friendly energy system: Application of Kalina cycle improved with fuel cell and thermoelectric module. *Process Saf. Environ. Prot.* **164**, 499–516 (2022).
49. Daniela-Abigail, H.-L. *et al.* Does recycling solar panels make this renewable resource sustainable? Evidence supported by environmental, economic, and social dimensions. *Sustain. Cities Soc.* <https://doi.org/10.1016/j.scs.2021.103539> (2021).
50. Tariq, R. *et al.* Projecting global water footprints diminution of a dew-point cooling system: Sustainability approach assisted with energetic and economic assessment. *Renew. Sustain. Energy Rev.* **140**, 110741 (2021).
51. Sarang, P., Kohli, H. P., Kumar, A. & Chakraborty, M. Artificial neural network approach towards the separation of ethylparaben and diclofenac using pseudo-emulsion hollow fiber strip dispersion technique. *Chem. Data Collect.* **40**, 100890 (2022).
52. Samadi-maybodi, A. & Nikou, M. Removal of sarafloxacin from aqueous solution by a magnetized metal-organic framework; artificial neural network modeling. *Polyhedron* **179**, 114342 (2020).
53. El-metwally, M. M., Abdel-fattah, G. M., Al-otibi, F. O. & Saber, W. I. A. Heliyon application of artificial neural networks for enhancing *Aspergillus flavipes* lipase synthesis for green biodiesel production. *Heliyon* **9**, e20063 (2023).
54. Sathishkumar, V. E., Ramu, A. G. & Cho, J. Machine learning algorithms to predict the catalytic reduction performance of eco-toxic nitrophenols and azo dyes contaminants (invited article). *Alex. Eng. J.* **72**, 673–693 (2023).
55. Georjin, J., Franco, D. S. P., Manzar, M. S., Meili, L. & El Messaoudi, N. A critical and comprehensive review of the current status of 17 β -estradiol hormone remediation through adsorption technology. *Environ. Sci. Pollut. Res.* **31**, 24679–24712 (2024).
56. Ahmad, T. *et al.* Enhanced adsorption of bisphenol-A from water through the application of isocyanurate based hyper crosslinked resin. *J. Mol. Liq.* **395**, 123861 (2024).
57. Gao, F., Xu, X. & Yang, J. Removal of p-nitrophenol from simulated sewage using MgCo-3D hydrotalcite nanospheres: Capability and mechanism. *RSC Adv.* **12**, 27044–27054 (2022).
58. Adebayo, M. A. & Areo, F. I. Removal of phenol and 4-nitrophenol from wastewater using a composite prepared from clay and *Cocos nucifera* shell: Kinetic, equilibrium and thermodynamic studies. *Resour. Environ. Sustain.* **3**, 100020 (2021).
59. Khan, H., Hussain, S., Fawad, S. & Gul, S. Environmental technology & innovation multivariate modeling and optimization of Cr (VI) adsorption onto carbonaceous material via response surface models assisted with multiple regression analysis and particle swarm embedded neural network. *Environ. Technol. Innov.* **24**, 101952 (2021).
60. Alatrasta, G., Pratt, C. & Hanandeh, A. E. Phosphate adsorption by metal organic frameworks: Insights from a systematic review, meta-analysis, and predictive modelling with artificial neural networks. *Chemosphere* **339**, 139674 (2023).
61. Aghav, R. M., Kumar, S. & Mukherjee, S. N. Artificial neural network modeling in competitive adsorption of phenol and resorcinol from water environment using some carbonaceous adsorbents. *J. Hazard. Mater.* **188**, 67–77 (2011).
62. Abatal, M., Anastopoulos, I., Giannakoudakis, D. A. & Olguin, M. T. Carbonaceous material obtained from bark biomass as adsorbent of phenolic compounds from aqueous solutions. *J. Environ. Chem. Eng.* **8**, 103784 (2020).
63. Alkurdi, S. S. A., Al-Juboori, R. A., Bundschuh, J., Bowtell, L. & Marchuk, A. Inorganic arsenic species removal from water using bone char: A detailed study on adsorption kinetic and isotherm models using error functions analysis. *J. Hazard. Mater.* **405**, 124112 (2021).
64. Patawat, C. *et al.* Preparation of activated carbon from *Dipterocarpus alatus* fruit and its application for. *RSC Adv.* **10**, 21082–21091 (2020).
65. Njewa, J. B., Vunain, E. & Biswick, T. Synthesis and characterization of activated carbons prepared from agro-wastes by chemical activation. *J. Chem.* **2022**, 1–13 (2022).

66. Ausavasukhi, A., Kamposoen, C. & Kengnok, O. Adsorption characteristics of congo red on carbonized leonardite. *J. Clean. Prod.* <https://doi.org/10.1016/j.jclepro.2015.10.034> (2015).
67. Li, Z. *et al.* Adsorption of congo red and methylene blue dyes on an ashitaba waste and a walnut shell-based activated carbon from aqueous solutions: Experiments, characterization and physical interpretations. *Chem. Eng. J.* **388**, 124263 (2020).
68. Maria, I., Manesco, R., Vieira, S. & Fernandes, M. Removal of tartrazine from aqueous solutions using adsorbents based on activated carbon and *Moringa oleifera* seeds. *J. Clean. Prod.* **171**, 85–97 (2018).
69. Beker, U., Ganbold, B., Dertli, H. & Güllbayir, D. D. Adsorption of phenol by activated carbon: Influence of activation methods and solution pH. *Energy Convers. Manag.* **51**, 235–240 (2010).
70. Nakamura, N., Yamamoto, T., Kobayashi, H. & Yoshimura, Y. The crystal and molecular structure of 1,18-dibromooctadecane. *Cryst. Res. Technol.* **28**, 953–957 (1993).
71. Huang, C. P. & Stumm, W. Specific adsorption of cations on hydrous γ - Al_2O_3 . *J. Colloid Interface Sci.* **43**, 409–420 (1973).
72. Kuśmierk, K. & Świątkowski, A. Adsorption of phenols on carbonaceous materials of various origins but of similar specific surface areas. *Separations* **10**, 422 (2023).
73. Khare, P. & Kumar, A. Removal of phenol from aqueous solution using carbonized *Terminalia chebula*-activated carbon: Process parametric optimization using conventional method and Taguchi's experimental design, adsorption kinetic, equilibrium and thermodynamic study. *Appl. Water Sci.* **2**, 317–326 (2012).
74. Aksu, Z. & Tezer, S. Equilibrium and kinetic modelling of biosorption of remazol black B by *Rhizopus arrhizus* in a batch system: Effect of temperature. *Process Biochem.* **36**, 431–439 (2000).
75. O'Mahony, T., Guibal, E. & Tobin, J. M. Reactive dye biosorption by *Rhizopus arrhizus* biomass. *Enzyme Microb. Technol.* **31**, 456–463 (2002).
76. Rincón-Silva, N. G., Moreno-Piraján, J. C. & Giraldo, L. Equilibrium, kinetics and thermodynamics study of phenols adsorption onto activated carbon obtained from lignocellulosic material (*Eucalyptus globulus* labill seed). *Adsorption* **22**, 33–48 (2016).
77. Ioannou, Z. & Simitzis, J. Adsorption kinetics of phenol and 3-nitrophenol from aqueous solutions on conventional and novel carbons. *J. Hazard. Mater.* **171**, 954–964 (2009).
78. Tshemese, S. J., Mhike, W. & Tichapondwa, S. M. Adsorption of phenol and chromium (VI) from aqueous solution using exfoliated graphite: Equilibrium, kinetics and thermodynamic studies. *Arab. J. Chem.* **14**, 103160 (2021).
79. Hameed, B. H., Tan, I. A. W. & Ahmad, A. L. Adsorption isotherm, kinetic modeling and mechanism of 2,4,6-trichlorophenol on coconut husk-based activated carbon. *Chem. Eng. J.* **144**, 235–244 (2008).
80. Nadeem, M., Shabbir, M., Abdullah, M. A., Shah, S. S. & McKay, G. Sorption of cadmium from aqueous solution by surfactant-modified carbon adsorbents. *Chem. Eng. J.* **148**, 365–370 (2009).
81. Hao, Z., Wang, C., Yan, Z., Jiang, H. & Xu, H. Magnetic particles modification of coconut shell-derived activated carbon and biochar for effective removal of phenol from water. *Chemosphere* **211**, 962–969 (2018).
82. Elsayed, I., Schueneman, G. T., El-Giar, E. M. & Hassan, E. B. Amino-functionalized cellulose nanofiber/lignosulfonate new aerogel adsorbent for the removal of dyes and heavy metals from wastewater. *Gels* **9**, 154 (2023).
83. Nikkhal, A. A., Zilouei, H., Asadinezhad, A. & Keshavarz, A. Removal of oil from water using polyurethane foam modified with nanoclay. *Chem. Eng. J.* **262**, 278–285 (2015).
84. Hamdaoui, O. Intensification of the sorption of rhodamine B from aqueous phase by loquat seeds using ultrasound. *Desalination* **271**, 279–286 (2011).
85. Ofomaja, A. E. & Ho, Y. S. Equilibrium sorption of anionic dye from aqueous solution by palm kernel fibre as sorbent. *Dyes Pigments* **74**, 60–66 (2007).
86. Hamad, B. K., Noor, A. M. & Rahim, A. A. Removal of 4-chloro-2-methoxyphenol from aqueous solution by adsorption to oil palm shell activated carbon activated with K_2CO_3 . *J. Phys. Sci.* **22**, 39–55 (2011).
87. Domínguez-Vargas, J. R., Navarro-Rodríguez, J. A., de Heredia, J. B. & Cuerda-Correa, E. M. Removal of chlorophenols in aqueous solution by carbon black low-cost adsorbents. Equilibrium study and influence of operation conditions. *J. Hazard. Mater.* **169**, 302–308 (2009).
88. Ren, L., Zhang, J., Li, Y. & Zhang, C. Preparation and evaluation of cattail fiber-based activated carbon for 2,4-dichlorophenol and 2,4,6-trichlorophenol removal. *Chem. Eng. J.* **168**, 553–561 (2011).
89. Gao, R. & Wang, J. Effects of pH and temperature on isotherm parameters of chlorophenols biosorption to anaerobic granular sludge. *J. Hazard. Mater.* **145**, 398–403 (2007).
90. Garba, Z. N. *et al.* An overview of chlorophenols as contaminants and their removal from wastewater by adsorption: A review. *J. Environ. Manag.* **241**, 59–75 (2019).
91. Gamboa, D. M. P. *et al.* Sorption behavior of azo dye congo red onto activated biochar from *Haematoxylum campechianum* waste: Gradient boosting machine learning-assisted Bayesian optimization for improved adsorption process. *Int. J. Mol. Sci.* **25**, 4771 (2024).
92. Zhang, C. *et al.* Leaf water content determination of oilseed rape using near-infrared hyperspectral imaging with deep learning regression methods. *Infrared Phys. Technol.* **134**, 104921 (2023).
93. Kang, I. K., Shin, T. Y. & Kim, J. H. Observation-informed modeling of artificial neural networks to predict flow and bleeding of cement-based materials. *Constr. Build. Mater.* **409**, 133811 (2023).
94. Hu, Y. & Kelly, H. International journal of hospitality management the dark side of artificial intelligence in service: The “watching-eye” effect and privacy concerns. *Int. J. Hosp. Manag.* **110**, 103437 (2023).
95. Alma, Y. V. *et al.* Biosorption of Pb(II) using natural and treated *Ardisia compressa* K. leaves: Simulation framework extended through the application of artificial neural network and genetic algorithm. *Molecules* **28**, 6387 (2023).
96. Asim, Y., Malik, A. K., Raza, B. & Shahid, A. R. A trust model for analysis of trust, influence and their relationship in social network communities. *Telemat. Inform.* **36**, 94–116 (2019).
97. Rosada, M. *et al.* Eight weeks of a lower limb resistance training protocol and gait performance in patients with symptomatic mild to moderate knee. *J. Orthop. Sci.* <https://doi.org/10.1016/j.jos.2023.07.007> (2023).
98. Abdallah, M. *et al.* Summer monsoon rainfall variations and its association with atmospheric circulations over Sudan. *J. Atmos. Sol. Terr. Phys.* **225**, 105751 (2021).
99. Isik, G. & van Sark, W. G. J. H. M. Predictive modeling of PV solar power plant efficiency considering weather conditions: A comparative analysis of artificial neural networks and multiple linear regression. *Energy Rep.* **10**, 2837–2849 (2023).
100. Li, K., Zhu, J., Ives, A. R., Radeloff, V. C. & Wang, F. Semiparametric regression for spatial data via deep learning. *Spat. Stat.* **57**, 100777 (2023).
101. Tariq, R., Ali, M., Sheikh, N. A., Shahzad, M. W. & Xu, B. B. Deep learning artificial intelligence framework for sustainable desiccant air conditioning system: Optimization towards reduction in water footprints. *Int. Commun. Heat Mass Transf.* **140**, 106538 (2023).
102. Shahade, A. K., Walse, K. H., Thakare, V. M. & Atique, M. Multi-lingual opinion mining for social media discourses: An approach using deep learning based hybrid fine-tuned smith algorithm with Adam optimizer. *Int. J. Inf. Manag. Data Insights* **3**, 100182 (2023).
103. Van Rossum, G., & Drake, F. L. Python 3 Reference Manual. Scotts Valley, CA: CreateSpace. <https://www.python.org/>. Accessed 29 Aug 2024. (2009).

104. Google LLC. Google Colaboratory. Available at: https://colab.research.google.com/?utm_source=scs-index. Accessed 29 Aug 2024 (2020).
105. Kim, B., Hwan, K. & Heo, S. Mean squared error criterion for model-based design of experiments with subset selection. *Comput. Chem. Eng.* **159**, 107667 (2022).
106. MathWorks. MATLAB: The Language of Technical Computing (Version R2023a) [Software]. Natick, Massachusetts: The MathWorks, Inc. Available at: <https://www.mathworks.com/products/matlab.html>. Accessed 29 Aug 2024. (2023).
107. Tariq, R. *et al.* Digital twin models for optimization and global projection of building-integrated solar chimney. *Build. Environ.* **213**, 108807 (2022).
108. Tariq, R., Torres-aguilar, C. E., Ahmed, N. & Ahmad, T. Data engineering for digital twinning and optimization of naturally ventilated solar façade with phase changing material under global projection scenarios. *Renew. Energy* **187**(1184), 1203 (2022).
109. Nadirgil, O. Carbon price prediction using multiple hybrid machine learning models optimized by genetic algorithm. *J. Environ. Manag.* **342**, 118061 (2023).

Acknowledgements

The authors would like to thank Tecnológico de Monterrey for the financial support provided through the 'Challenge-Based Research Funding Program 2023', Project ID #IJXT070-23EG99001, entitled 'Complex Thinking Education for All (CTE4A): A Digital Hub and School for Lifelong Learners.'

Author contributions

All authors have contributed in all the parts from the conceptualization to the formal analysis and the write up of the article.

Competing interests

The authors declare no competing interests.

Additional information

Supplementary Information The online version contains supplementary material available at <https://doi.org/10.1038/s41598-024-70989-0>.

Correspondence and requests for materials should be addressed to M.A.

Reprints and permissions information is available at www.nature.com/reprints.

Publisher's note Springer Nature remains neutral with regard to jurisdictional claims in published maps and institutional affiliations.

Open Access This article is licensed under a Creative Commons Attribution-NonCommercial-NoDerivatives 4.0 International License, which permits any non-commercial use, sharing, distribution and reproduction in any medium or format, as long as you give appropriate credit to the original author(s) and the source, provide a link to the Creative Commons licence, and indicate if you modified the licensed material. You do not have permission under this licence to share adapted material derived from this article or parts of it. The images or other third party material in this article are included in the article's Creative Commons licence, unless indicated otherwise in a credit line to the material. If material is not included in the article's Creative Commons licence and your intended use is not permitted by statutory regulation or exceeds the permitted use, you will need to obtain permission directly from the copyright holder. To view a copy of this licence, visit <http://creativecommons.org/licenses/by-nc-nd/4.0/>.

© The Author(s) 2024